



**HAL**  
open science

## Reconciliation of asynchronous satellite-based NO<sub>2</sub> and XCO<sub>2</sub> enhancements with mesoscale modeling over two urban landscapes

Ruixue Lei, Sha Feng, Yang Xu, Sophie Tran, Michel Ramonet, Michel Grutter, Agustin Garcia, Mixtli Campos-Pineda, Thomas Lauvaux

### ► To cite this version:

Ruixue Lei, Sha Feng, Yang Xu, Sophie Tran, Michel Ramonet, et al.. Reconciliation of asynchronous satellite-based NO<sub>2</sub> and XCO<sub>2</sub> enhancements with mesoscale modeling over two urban landscapes. Remote Sensing of Environment, 2022, 281, pp.113241. 10.1016/j.rse.2022.113241 . hal-03790703

**HAL Id: hal-03790703**

**<https://hal.science/hal-03790703>**

Submitted on 28 Sep 2022

**HAL** is a multi-disciplinary open access archive for the deposit and dissemination of scientific research documents, whether they are published or not. The documents may come from teaching and research institutions in France or abroad, or from public or private research centers.

L'archive ouverte pluridisciplinaire **HAL**, est destinée au dépôt et à la diffusion de documents scientifiques de niveau recherche, publiés ou non, émanant des établissements d'enseignement et de recherche français ou étrangers, des laboratoires publics ou privés.



Distributed under a Creative Commons Attribution 4.0 International License



# Reconciliation of asynchronous satellite-based NO<sub>2</sub> and XCO<sub>2</sub> enhancements with mesoscale modeling over two urban landscapes

Ruixue Lei<sup>a,b,\*</sup>, Sha Feng<sup>a,c,\*\*</sup>, Yang Xu<sup>d</sup>, Sophie Tran<sup>d</sup>, Michel Ramonet<sup>d</sup>, Michel Grutter<sup>e</sup>, Agustín García<sup>e</sup>, Mixtli Campos-Pineda<sup>e</sup>, Thomas Lauvaux<sup>d,f</sup>

<sup>a</sup> Department of Meteorology and Atmospheric Science, The Pennsylvania State University, University Park, PA, USA

<sup>b</sup> Department of Environmental Health and Engineering, Johns Hopkins University, Baltimore, MD, USA

<sup>c</sup> Atmospheric Sciences and Global Change Division, Pacific Northwest National Laboratory, Richland, WA, USA

<sup>d</sup> LSCE, CEA, CNRS, UVSQ/IPSL, Université Paris-Saclay, Orme des Merisiers, Gif sur Yvette 91191, France

<sup>e</sup> Instituto de Ciencias de la Atmósfera y Cambio Climático, Universidad Nacional Autónoma de México, Mexico City, Mexico

<sup>f</sup> GSMA, University of Reims-Champagne Ardenne, UMR CNRS 7331, Reims, France

## ARTICLE INFO

Edited by Menghua Wang

### Keywords:

OCO-3 SAMs  
TROPOMI  
WRF-Chem  
Washington D.C.-Baltimore  
Mexico City

## ABSTRACT

Fossil fuel carbon dioxide (CO<sub>2ff</sub>), the main driver of global warming and climate change, is often co-emitted with nitrogen oxides (NO<sub>x</sub>) and precursors to ground-level ozone from anthropogenic sources like power plants or vehicles. In urban and suburban areas, satellite-based NO<sub>2</sub> can be used as a proxy to track the emissions of CO<sub>2ff</sub>. Because of NO<sub>2</sub>'s shorter lifetime, urban NO<sub>2</sub> plumes are more distinguishable from backgrounds and more sensitive to variations in emissions. However, the combination of these two gases is limited by the asynchrony among NO<sub>2</sub> and CO<sub>2</sub> monitoring satellites. We used CO<sub>2ff</sub> simulated by the Weather Research and Forecasting model coupled with Chemistry (WRF-Chem) model to reconcile the tropospheric NO<sub>2</sub> vertical column density (VCD) from Tropospheric Monitoring Instrument (TROPOMI) and column-averaged dry-air mole fractions of carbon dioxide enhancements (ΔXCO<sub>2</sub>) from Orbiting Carbon Observatory 3 (OCO-3) Snapshot Area Maps (SAMs) over a multicity area, Washington D.C.-Baltimore (DC-Balt), and a basin city, Mexico City. NO<sub>2</sub>/CO<sub>2ff</sub> ratios over DC-Balt are smaller than Mexico City, indicative of stricter emission restrictions, a more combustion-efficient vehicle fleet, and higher combustion efficiency due to lower altitude in DC-Balt. For single-track cases, the spatial correlations between NO<sub>2</sub> and ΔXCO<sub>2</sub> over Mexico City are stronger than DC-Balt because the NO<sub>2</sub> and CO<sub>2</sub> are mostly trapped in the valley of Mexico City, while DC-Balt is severely affected by distant sources (i. e., US East Coast cities). Using multi-track averaging, spatial correlation coefficients increase with the number of days used for averaging. The correlations reached a maximum when averaging >12 continuous images for DC-Balt and >10 continuous images for Mexico City. This finding indicates that multi-track averaging using modeled CO<sub>2ff</sub> as a proxy is helpful to filter the noise in single-track images, to cancel the interference from distant sources, and to magnify correlations between NO<sub>2</sub> and CO<sub>2ff</sub>. Mexico City showed stronger spatial correlations but weaker temporal correlations than DC-Balt due to biomass burning hot spots and large transport errors caused by the trapping effects of the surrounding mountains. Tracking the 20-day moving average of CO<sub>2ff</sub> emissions using TROPOMI NO<sub>2</sub> seems technically feasible, considering the relationship between correlation coefficients and the number of available satellite images.

## 1. Introduction

Oxides of nitrogen (NO<sub>x</sub>), precursors to ground-level ozone, and fossil fuel carbon dioxide (CO<sub>2ff</sub>), the main driver of global warming and climate change (IPCC, 2014; UNFCCC, 2015) are often co-emitted from

anthropogenic sources like power plants or vehicles (Hakkariainen et al., 2021), usually concentrated in urban and suburban areas. Global CO<sub>2ff</sub> emissions exceeded 38 Gt in 2020 (Crippa et al., 2020) accounting for >77% of fossil fuel greenhouse gas emissions (Crippa et al., 2019) and >70% originate from cities alone (Birol, 2008; Mitchell et al., 2018).

\* Corresponding author at: Department of Environmental Health and Engineering, Johns Hopkins University, Baltimore, MD, USA.

\*\* Corresponding author at: Atmospheric Sciences and Global Change Division, Pacific Northwest National Laboratory, Richland, WA, USA.

E-mail addresses: [rlei3@jhu.edu](mailto:rlei3@jhu.edu) (R. Lei), [sfeng@pnnl.gov](mailto:sfeng@pnnl.gov) (S. Feng).

<https://doi.org/10.1016/j.rse.2022.113241>

Received 30 December 2021; Received in revised form 25 August 2022; Accepted 26 August 2022

Available online 13 September 2022

0034-4257/© 2022 The Authors. Published by Elsevier Inc. This is an open access article under the CC BY-NC-ND license (<http://creativecommons.org/licenses/by-nc-nd/4.0/>).

Global NO<sub>x</sub> emissions exceeded 55 TgN in 2019 (Miyazaki et al., 2021), predominantly emitted from vehicles in urban areas (Chavez-Baeza and Sheinbaum-Pardo, 2014; Parrish et al., 2009). CO<sub>2ff</sub> and NO<sub>x</sub> spatial and temporal correlations have been widely studied (Ammoura et al., 2014; Hakkarainen et al., 2021; Kuhlmann et al., 2019; Lopez et al., 2013; Park et al., 2021; Reuter et al., 2014) and utilized in emission quantification (Berezin et al., 2013; Reuter et al., 2019; Zheng et al., 2020) and co-benefits analysis (Dong et al., 2015; Qian et al., 2021; Xie et al., 2018).

Bottom-up approaches used to estimate anthropogenic NO<sub>x</sub> and CO<sub>2</sub> emissions have achieved high spatial resolution (0.1° × 0.1°) thanks to downscaling techniques using proxies like population density (e.g., MIX; Li et al., 2017), nighttime lights (e.g., ODIAC; Oda et al., 2018), or combinations of point sources like power plants (e.g., PKU-Fuel; Wang et al., 2013) and line sources for on-road emissions (e.g., HESTIA; Gurney et al., 2018). But uncertainties in nationwide annual bottom-up fossil fuel can be large, ranging from 5% in Organization for Economic Co-operation and Development (OECD) countries (Marland, 2008), to 25% for China (Shan et al., 2018), to 50% or more for emerging economies (Andres et al., 2014). As for temporal resolution, daily and near real-time bottom-up estimations using activity data and energy use indicators have recently emerged (Liu et al., 2020a), but it is still challenging to retrieve reliable near real-time statistics of sector-specific fossil fuel consumption and match independent atmospheric observations (Dou et al., 2021a).

Satellite-based inversions combine satellite observations with atmospheric transport models and (or) bottom-up emissions to estimate the sources and sinks of greenhouse gases (Crowell et al., 2019; Lei et al., 2021; Ye et al., 2020). Currently, estimation of NO<sub>x</sub> emissions from satellite observations is generally easier than for CO<sub>2ff</sub> for several reasons: (1) the lifetime of NO<sub>x</sub> is much shorter than CO<sub>2</sub> (several hours vs. hundred years), making local NO<sub>x</sub> signals more distinguishable from background values and more sensitive to variations in emissions than CO<sub>2</sub>; (2) CO<sub>2ff</sub> signals need to be separated from biogenic signals before inversion (Ye et al., 2020) while NO<sub>x</sub> is mainly from the anthropogenic sources in urban areas (Zhang et al., 2003); and (3) the available NO<sub>2</sub> satellite observations are more frequent than CO<sub>2</sub> thanks to shorter revisit times and a broader spatial coverage. Consequently, satellite-based NO<sub>x</sub> emission estimations over cities and large point sources benefit from averaging multiple tracks (Goldberg et al., 2019a; Saw et al., 2021), while CO<sub>2</sub> emission estimations are often based on individual overpasses (Nassar et al., 2017; Yang et al., 2020; Ye et al., 2020).

The need for satellite monitoring of carbon emissions has become more pressing than ever (Bézy et al., 2019). The world's major economies have pledged to achieve carbon neutrality by 2050 (Paris Agreement, UNFCCC, 2015), and the COVID-19 pandemic caused a temporary reduction in global carbon emissions (Liu et al., 2020b). Current CO<sub>2</sub> satellites alone cannot detect long-term CO<sub>2ff</sub> emission trends (Lei et al., 2021) or daily variations (Liu et al., 2020b). Therefore, recent studies used NO<sub>2</sub> as a proxy of anthropogenic CO<sub>2</sub> to achieve better spatial and temporal resolutions (Dou et al., 2021b; Kuhlmann et al., 2019; Zheng et al., 2020). In these studies, satellite measurements of NO<sub>2</sub> are converted to NO<sub>x</sub> emissions using a fixed factor of 1.33 derived from long-term statistics (Goldberg et al., 2019b, 2019a) (a simplification of the complex urban chemistry of aerosols; Atkinson, 2000), or pre-calculated NO<sub>x</sub>/NO<sub>2</sub> ratios (Lorente et al., 2019; Zheng et al., 2020). CO<sub>2ff</sub> emissions are then calculated based on NO<sub>x</sub>/CO<sub>2</sub> ratios based on emission factors and consumptions of different types of fuels. But the effects of meteorology, sectoral energy use, and anthropogenic activity on NO<sub>2</sub>/NO<sub>x</sub> ratios should not be ignored when investigating short-term variations of emissions. Additionally, previous studies relied on NO<sub>2</sub> and CO<sub>2</sub> satellites in orbits with a very close local solar time to avoid the problem of asynchronous overpassing (Reuter et al., 2019), which cannot be circumvented for all CO<sub>2</sub> and NO<sub>2</sub> satellites. Last but not least, most studies (Beirle et al., 2021; Goldberg et al., 2019a; Nassar et al., 2021, 2017; Reuter et al., 2019) are focused on power plants or isolated cities with clean backgrounds with little interference from distant sources;

Schuh et al. (2021) have quantified variations from large-scale CO<sub>2</sub> inflow limiting our ability to detect and quantify city plumes.

To understand the representativity of satellite-based NO<sub>2</sub> as a proxy of CO<sub>2ff</sub> across different cities, we investigated spatial and temporal correlations between NO<sub>2</sub> vertical column density (VCD) from TROPOMI and column-average CO<sub>2</sub> dry-air mole fraction enhancement (ΔXCO<sub>2</sub>) from OCO-3 SAMs over two typical metropolitan areas: Washington D.C.-Baltimore (DC-Balt) and Mexico City. We compared satellite data with model concentrations from WRF-Chem to reconcile the asynchrony of the two satellites. In Section 2, we describe the data and methodology. We evaluate discrepancies between NO<sub>2</sub> and ΔXCO<sub>2</sub> spatial distributions for single tracks in Section 3.1. Then we evaluate the role of various averaging time windows (multitrack analysis) to help reconcile model-data discrepancies and to quantify temporal variations of NO<sub>2</sub> and ΔXCO<sub>2</sub> in Section 3.2. Finally, we discuss the results in Section 4 and conclude in Section 5.

## 2. Data and method

We selected two representative metropolitan areas, DC-Balt and Mexico City, which are challenging for atmospheric CO<sub>2</sub> modeling in terms of urban boundaries (DC-Balt) and terrain (Mexico City). DC-Balt is located on the East Coast of the US on relatively flat terrain; thus, it is a typical multicentric region as described in Ye et al. (2020). Unlike isolated plume cities, DC-Balt is affected by CO<sub>2</sub> plumes originating from upwind power plants from places like the Ohio river valley and other large cities on the East coast of the United States (e.g., Philadelphia, New York, and Richmond). Mexico City is a typical "basin city" whose terrain resembles Los Angeles, as shown in Ye et al. (2020). Because of complex topography, the simulated CO<sub>2</sub> spatial distribution over the city is more sensitive to transport model errors. CO<sub>2ff</sub> emissions from DC-Balt are about 20.5 TgC/year, and the on-road sector (mostly traffic) dominates the city emissions over DC-Balt, accounting for about 45% of the annual total (Yadav et al., 2021). The electricity production sector in DC-Balt is the second most important contributor, accounting for 19% of annual emissions, although this contribution can vary throughout the year depending on the heating and cooling demand. Total CO<sub>2ff</sub> emissions from Mexico City are about 21 TgC/year as reported by Emission Inventory for Mexico City-2016 (SEDEMA, 2018), about 76.8% of which are emitted by mobile sources. >4.2 million passenger vehicles represent 61% of criteria pollutants and 44% of GHG (greenhouse gas) emissions (Chavez-Baeza and Sheinbaum-Pardo, 2014).

### 2.1. Case selection

We firstly selected several individual cases of asynchronous satellite-based NO<sub>2</sub> and ΔXCO<sub>2</sub> according to data integrity and the co-existence of tropospheric column NO<sub>2</sub> from TROPOMI and XCO<sub>2</sub> from OCO-3 Snapshot Area Maps (SAMs) mode. The description of OCO-3 and TROPOMI retrievals is available in Section 2.2. We scanned all the available OCO-3 SAMs (available mostly from January to June 2020) and selected three cases over DC-Balt and six cases over Mexico City. XCO<sub>2</sub> maps (filtered by quality\_flag = 0) in OCO-3 SAMs show clear spatial gradients of 1.5 ppm above background. The NO<sub>2</sub> retrievals selected here correspond to the highest quality measurements (quality assurance flag (QA\_flag) > 0.75) as recommended by Goldberg et al. (2021) and cover >50% of our study areas.

Then we selected February 2020 as our study period for our multiday averaging experiment. February 2020 is a cold month for DC-Balt and Mexico City, when NO<sub>2</sub> lifetime is relatively long (limited chemical production and destruction), and biogenic CO<sub>2</sub> signals are weaker than warm months. Hence, this period is better suited to establish a relationship between anthropogenic CO<sub>2</sub> and NO<sub>2</sub> than during warm months with high photochemistry. Furthermore, mobility restrictions causing a reduction in emissions of CO<sub>2</sub> and NO<sub>2</sub> during the COVID-19 pandemic (Liu et al., 2020) occurred later, in mid-March. We selected 17 and 16

TROPOMI NO<sub>2</sub> images (filtered by the same criteria used for individual cases) over DC-Balt and Mexico City, respectively. Due to the lack of OCO-3 SAMs XCO<sub>2</sub> data, we use XCO<sub>2ff</sub> simulated by WRF-Chem as a proxy of XCO<sub>2</sub> enhancements ( $\Delta XCO_2$ ) from OCO-3 SAMs mode. To validate these simulated XCO<sub>2ff</sub> fields, we compared WRF-Chem XCO<sub>2ff</sub> to high-accuracy ground-based CO<sub>2</sub> measurements and OCO-3  $\Delta XCO_2$  from SAMs in Section 2.3.4.

## 2.2. Satellite data

OCO-3 was launched on May 4, 2019, and started to collect XCO<sub>2</sub> data on September 6, 2019. OCO-3 instrumentation is similar to that of OCO-2, but pointing capabilities offer unique images (SAMs mode) that cover wider regions compared to traditional nadir and glint modes, by collecting multiple swaths using the agile 2-axis pointing mirror assembly (PMA). We use the OCO-3 version 10r L2 lite product recently publicly available through the NASA Goddard Earth Science Data and Information Services Center (GES DISC) (<http://disc.sci.gsfc.nasa.gov/>). This product uses the newest Atmospheric Carbon Observations from Space (ACOS, O'Dell et al., 2018) build 10 (b10) software suite using an early Ancillary Radiometric Product (ARP). The performance of the OCO-3 early version (vEarly) was first evaluated over the Los Angeles megacity by Kiel et al. (2021).

TROPOMI was launched on October 13, 2017, with quality-controlled data made available since April 30, 2018. We downloaded NO<sub>2</sub> data through the European Space Agency (ESA) for the European Union's Copernicus Sentinel 5 Precursor (S5p) satellite mission (<http://www.tropomi.eu/data-products/data-access>). TROPOMI operates in a sun-synchronous polar orbit nominally crossing the equator at approximately 13:30 local solar time. TROPOMI NO<sub>2</sub> VCD has been compared to XCO<sub>2</sub> from OCO-2 (Nassar et al., 2021; Reuter et al., 2019) (overpassing at 13:36 local solar time) thanks to near-synchronous overpassing times. Note that OCO-3 onboard the International Space Station (Eldering et al., 2019; Taylor et al., 2020) no longer follows sun-synchronous polar orbit as OCO-2 and TROPOMI. Here we intend to reconcile the asynchronous satellite-based NO<sub>2</sub> and  $\Delta XCO_2$  with meso-scale modeling, validated with ground-based in situ measurements, as described in Section 2.3.4. Low biases in TROPOMI NO<sub>2</sub> data have been detected and estimated using aircraft (Judd et al., 2020) and ground-based data (van Geffen et al., 2022), possibly due to the cloud algorithm, a priori NO<sub>2</sub> profiles, and coarse-resolution surface reflectivity. Here, we sampled city plumes beyond city limits and therefore expect low biases in NO<sub>2</sub> retrievals. The original tropospheric NO<sub>2</sub> unit in TROPOMI data and CO<sub>2</sub> unit in OCO-3 data are mol/m<sup>2</sup> and ppm, respectively. To intuitively compare them, we converted mol/m<sup>2</sup> into ppb (10<sup>-3</sup> ppm) using Eqs. (1) and (2):

$$VCD_{air\_tropo} = 1/g/M_{air} \times (p_{sfc} - p_{tropo}) \times 1000 - SCD_{water}/AMF \quad (1)$$

$$XNO_{2\_tropo} = VCD_{no2\_tropo}/VCD_{air\_tropo} \times 10^9 \quad (2)$$

Where  $VCD_{air\_tropo}$  is the tropospheric vertical column density of dry air in the unit of mol/m<sup>2</sup>.  $g$  is the gravity acceleration constant, known as 9.8 m/s<sup>2</sup>,  $M_{air}$  is the molecular weight of air, set as 29 g/mol.  $p_{sfc}$  is the air pressure at the surface in the unit of Pa.  $p_{tropo}$  is the air pressure at the tropopause in the unit of Pa.  $SCD_{water}$  is the water slant column density in the unit of mol/m<sup>2</sup>. TROPOMI only provides the water density in the total slant column. We assume that most water is in the troposphere.  $AMF$  is the air mass factor, converting slant column density to vertical column density.  $XNO_{2\_tropo}$  is the tropospheric column averaged mixing ratio of NO<sub>2</sub> in the unit of ppb.  $VCD_{no2\_tropo}$  is the vertical column density of NO<sub>2</sub> in the unit of mol/m<sup>2</sup>.

## 2.3. WRF-chem setup

We simulated CO<sub>2</sub> mole fractions to generate  $\Delta XCO_2$  using WRF-

Chem V3.6.1 (Grell et al., 2005; Skamarock et al., 2008) with CO<sub>2ff</sub> emissions and biospheric CO<sub>2</sub> fluxes in passive tracer mode (Lauvaux et al., 2012). The WRF-Chem configuration (domain size, resolution, physics schemes) is described in Ye et al. (2020) and Lei et al. (2021).

### 2.3.1. Atmospheric transport model setup

We use one-way nested domains with resolutions of 9- and 3-km for both cities (Fig. 1). For DC-Balt, the 9-km outer domain is set to 71.92–82.10°W, 35.03–42.96°N, ~900 km × 900 km, which includes some metropolitan areas in northeast US (e.g., New York in NY, Philadelphia and Pittsburgh in PA, Cleveland in OH, Charlotte in NC, and DC-Balt), and part of Lake Erie and the North Atlantic Ocean. The inner 3-km domain is set to 75.2–78.4°W, 37.20–39.90°N, ~330 km × 330 km. This domain centers on DC-Balt and covers the nearby urban areas (i.e., part of Wilmington in Delaware and Richmond in Virginia) and most of the Chesapeake Bay. For Mexico City, the outer domain is set to 90.03–108.32°W, 13.88–24.72°N, ~1900 km × 1200 km, which includes the South of Mexico, western Guatemala, part of the Gulf of Mexico, and the North Pacific Ocean. The inner 3-km domain is set to 97.47–100.79°W, 18.15–20.95°N, of ~350 km × 320 km in size, which centers on Mexico City and covers the nearby provinces.

The WRF-Chem simulations are driven by the hourly ERA5 reanalysis data (Hersbach et al., 2020) on 0.25° × 0.25° grids which are also used as the initial and boundary conditions of the meteorological and land surface fields. A total of 51 vertical levels are set to represent the atmospheric column from the surface to 50 hPa. At urban scale, long-range transport of CO<sub>2</sub> generates only large-scale spatial gradients, which preserve the local enhancements; therefore, the initial and boundary conditions for the CO<sub>2</sub> mole fractions are set constant. Each simulation runs for 84 h starting at 00:00 UTC 3 days before the OCO-3 and TROPOMI overpassing times, including a spin-up time of 12 h. To minimize the XCO<sub>2</sub> errors caused by model transport errors, the simulations are nudged to ERA5 using grid nudging.

### 2.3.2. Biogenic CO<sub>2</sub> fluxes

For DC-Balt, biogenic CO<sub>2</sub> fluxes are based on hourly Net Ecosystem Exchange (NEE) of CO<sub>2</sub> from the Vegetation Photosynthesis and Respiration Model (VPRM) (Mahadevan et al., 2008), a satellite-based assimilation scheme of 12 North American biomes using the Enhanced Vegetation Index (EVI) and Land Surface Water Index (LSWI), derived from reflectance from the Moderate Resolution Imaging Spectroradiometer (MODIS), plus high-resolution sunlight and air temperature data. The VPRM NEE data at 0.02° × 0.02° were provided over the first 6 months of 2020 (Gourdji et al., 2021) and regridded over the WRF-Chem domains using bi-linear interpolation.

For Mexico City, we use the NEE product Gridded Ensembles of Surface Biogenic Carbon Fluxes (Zhou et al., 2020) from an ensemble of Carnegie Ames Stanford Approach (CASA) model simulations. This ensemble provides CO<sub>2</sub> biogenic fluxes and their uncertainties at 3-hourly time scales over 2003–2019 on a 463-m spatial resolution grid for the conterminous United States (CONUS) and on both 5-km and half-degree spatial resolution grids for North America. The biogenic CO<sub>2</sub> enhancement is much smaller than fossil fuel CO<sub>2</sub> enhancement near the urban area (Lei et al., 2021), and the average temperature difference in the first half of the years 2019 and 2020 is <1 °C (<https://www.wunderground.com/weather/mx/mexico-city/MMMX>); thus, we assume that CO<sub>2</sub> biogenic fluxes in February 2020 can be represented by CASA biogenic fluxes from 2019 thanks to the reduced vegetation activity in winter. The 3-hourly 5-km fluxes are linearly interpolated to 1-hly then regridded to WRF-Chem domain resolutions using bi-linear interpolation.

### 2.3.3. Fossil fuel CO<sub>2</sub> emissions

For DC-Balt, we coupled the CO<sub>2ff</sub> emissions of the Vulcan project version 3.0 (Gurney et al., 2019) available from 2010 to 2015 to the WRF-Chem model. The Vulcan product is the first bottom-up inventory

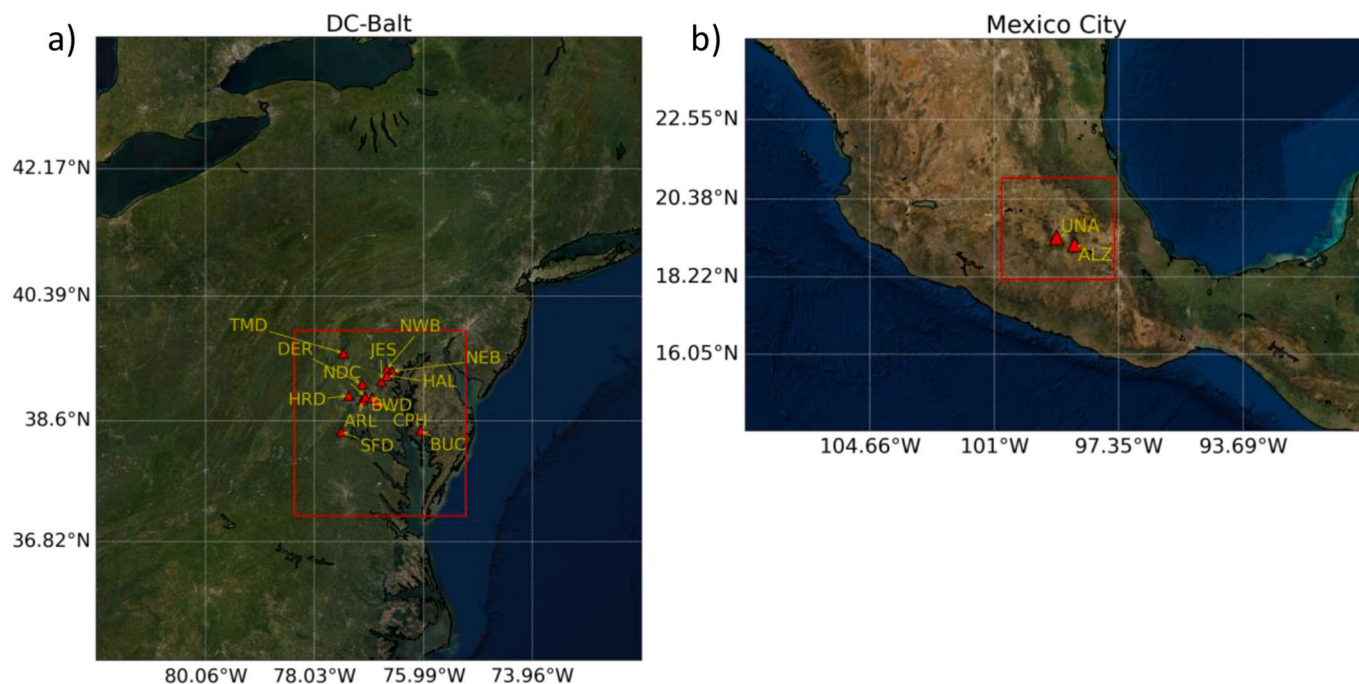


**Fig. 1.** Domain settings and in situ site locations in (a) DC-Balt and (b) Mexico City. The whole maps show the range of the outer domain. The red rectangles show the range of the inner domain. The red triangles show the locations of in situ sites. (For interpretation of the references to colour in this figure legend, the reader is referred to the web version of this article.)

to report  $\text{CO}_{2\text{ff}}$  plus cement production  $\text{CO}_2$  fluxes at 1-hour and 1-km resolution for all major carbon-emitting sectors for the CONUS and the State of Alaska. The Vulcan emissions are categorized into 10 source sectors including residential, commercial, industrial, electricity production, onroad, nonroad, commercial marine vessel, airport, rail, and cement. The annual anthropogenic  $\text{CO}_2$  emission over DC-Balt only increased by 1.1% from 2015 to 2020 based on CAMS-GLOB-ANT V4.2 (<https://ads.atmosphere.copernicus.eu/cdsapp#!/dataset/cams-global-emission-inventories?tab=overview>). Thus, we assume that  $\text{CO}_2$  diurnal and monthly variations in 2020 remain the same as the corresponding weekday/weekend of the year 2015. We also regridded the 1-hourly  $\text{CO}_{2\text{ff}}$  emissions to WRF-Chem domain resolutions using bi-linear interpolation.

For Mexico City, fossil fuel  $\text{CO}_2$  emissions are based on Mexican National Emissions Inventory (NEI, <https://www.gob.mx/semarnat/documentos/documentos-del-inventario-nacional-de-emisiones>) for the year 2016. Considering an annual population growth rate of about 0.4%, we also assume that the emissions remain nearly constant by 2020. In the NEI 2016, the emissions of  $\text{CO}_2$  are from the Mexico City Emissions Inventory (SEDEMA, 2018) based on the same activity information used for producing the criteria pollutant emissions. The emissions activity categories are ground transport, airport, solid waste, wastewater, residential combustion, and cattle raising. This emission inventory for criteria pollutants has been evaluated by Rodríguez Zas and García Reynoso (2021) and Maldonado-Pacheco et al. (2021). We generated the  $\text{CO}_{2\text{ff}}$  emission inputs for WRF-Chem by using a program developed by the National Autonomous University of Mexico (UNAM) which is publicly available through GitHub ([https://github.com/JoseAgustin/emis\\_2016](https://github.com/JoseAgustin/emis_2016)).

#### 2.3.4. Model validation

This study focuses on afternoon  $\text{CO}_2$  enhancements, at TROPOMI overpassing time. At that time, model performances reach their best scores when  $\text{CO}_2$  is well mixed in the atmospheric boundary layer. To establish model performances, we compare daily afternoon (12:00–17:00 local time)  $\text{CO}_2$  enhancements extracted from WRF-Chem

outputs with ground-based high-accuracy in situ  $\text{CO}_2$  measured by Picarro Cavity Ring-Down Spectroscopic (CRDS) analyzers (Rella et al., 2013). Fig. 2 shows the comparison of our 1-month simulation for February 2020 and Fig. S1 shows the comparison for individual OCO-3 SAMs cases selected in Section 2.1. We also compared the model wind speeds and directions with NCAR Upper Air Database (NCAR, 2014) (Fig. S2-S5).

For DC-Balt, we use  $\text{CO}_2$  measurements collected from 13 towers (locations shown in Fig. 1a) in the WRF-Chem inner domain, part of the North-East Corridor Baltimore/Washington Project (Karion et al., 2020). We selected different background sites at different hours based on wind directions. We calculated the mean wind direction at each hour based on WRF-Chem horizontal mean wind components at 3-km resolution, then we selected the tower at the far end of the network, upwind relative to the city, as the background site. The  $\text{CO}_2$  enhancement for both the model and observations is defined as the difference in  $\text{CO}_2$  mole fractions between each tower and the selected background site.

For Mexico City, we used ground-based in situ high-accuracy  $\text{CO}_2$  measurements published by (del Castillo et al., 2020), collected from the top of a three-story building on the eastern edge of the UNAM main campus (19.3262 N, 99.1761 W, 2280 m a.s.l., 13 km south from the city center) and at a high-altitude station located at Altzomoni (19.1187 N, 98.6552 W, 3985 m a.s.l., 60 km southeast from the UNAM site) (locations shown in Fig. 1b). The  $\text{CO}_2$  enhancement is defined as the difference in  $\text{CO}_2$  mole fractions between these two sites.

The WRF-Chem model successfully replicates the hourly variations in  $\text{CO}_2$  enhancements shown by in situ sites for both cities (Fig. 2ab). The comparison of daily afternoon average  $\text{CO}_2$  enhancements confirms the model's capabilities to represent spatial gradients over multiple days for both cities (Fig. 2cd). In general,  $\text{CO}_2$  enhancements simulated by WRF-Chem in DC-Balt are slightly larger than observed in situ measurements, while  $\text{CO}_2$  enhancements over Mexico City are slightly lower than in situ measurements on average. The coefficient of determination ( $R^2$ ) for  $\text{CO}_2$  mole fractions across DC-Balt (0.44) is smaller than Mexico City (0.51).

As for wind evaluation (Fig. S2-S5), the WRF-Chem model underestimates wind speed by 0.22 m/s over DC-Balt and overestimates by

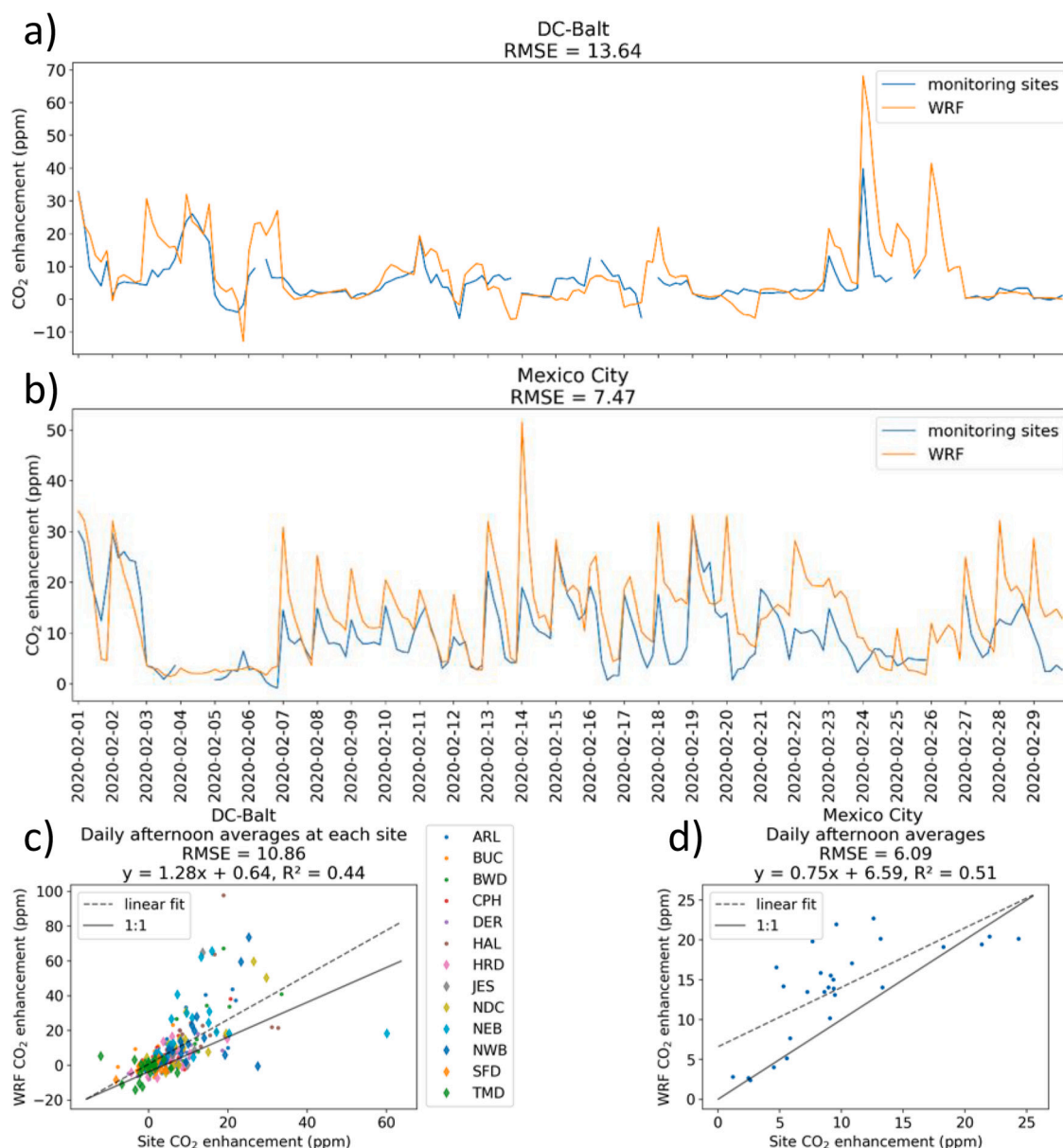


**Fig. 2.** Comparison of afternoon CO<sub>2</sub> enhancement in February 2020 between WRF and in-situ site measurements: (a) time series of hourly averaged enhancements of all in-situ sites in DC-Balt; (b) time series of hourly enhancements in Mexico City; (c) scatters of daily afternoon averages in DC-Balt. The dots and diamonds in different colors represent the different sites; (d) scatters of daily afternoon averages in Mexico City. Note: The blue lines in (a) and (b) are not continuous due to missing data. There are 13 sites in DC-Balt, resulting in 12 enhancement values per hour, while there are two sites in Mexico City, resulting in only one enhancement value per hour, as one site is selected as the background site in each hour. For DC-Balt, enhancement can be negative because the background site chosen by wind direction is not the lowest CO<sub>2</sub>. (For interpretation of the references to colour in this figure legend, the reader is referred to the web version of this article.)

1.23 m/s over Mexico City at heights of 700 and 800 hPa. At heights below 700 hPa, the WRF-Chem overestimates wind speed by 0.52 m/s over DC-Balt and 3.37 m/s over Mexico City. The mean wind direction biases are 4.05° over DC-Baltimore and 14.31° over Mexico City at heights of 700 and 800 hPa. At heights below 700 hPa, the wind direction biases are 1.20° over DC-Baltimore and 34.02° over Mexico City. In general, the WRF-Chem performance at high altitudes is better than near-surface. The performance over Mexico City is worse than over DC-Balt due to the interference of mountains near Mexico City.

### 3. Results

#### 3.1. Comparison between WRF-Chem outputs and satellite observations for single tracks

OCO-3  $\Delta$ XCO<sub>2</sub> should not be directly compared with TROPOMI NO<sub>2</sub> considering the differences in overpass time and interferences from other sources (e.g., background, biogenic fluxes). Instead, we compared WRF-Chem XCO<sub>2</sub> with OCO-3 XCO<sub>2</sub> at the exact overpassing time of OCO-3 to test whether WRF-Chem is a good proxy of OCO-3, then compared WRF-Chem XCO<sub>2ff</sub> and TROPOMI NO<sub>2</sub> at the exact overpassing time of TROPOMI to study the correlation between XCO<sub>2</sub> enhancements and NO<sub>2</sub>.

Fig. 3 shows XCO<sub>2</sub> from WRF-Chem and OCO-3 over DC-Balt for 13

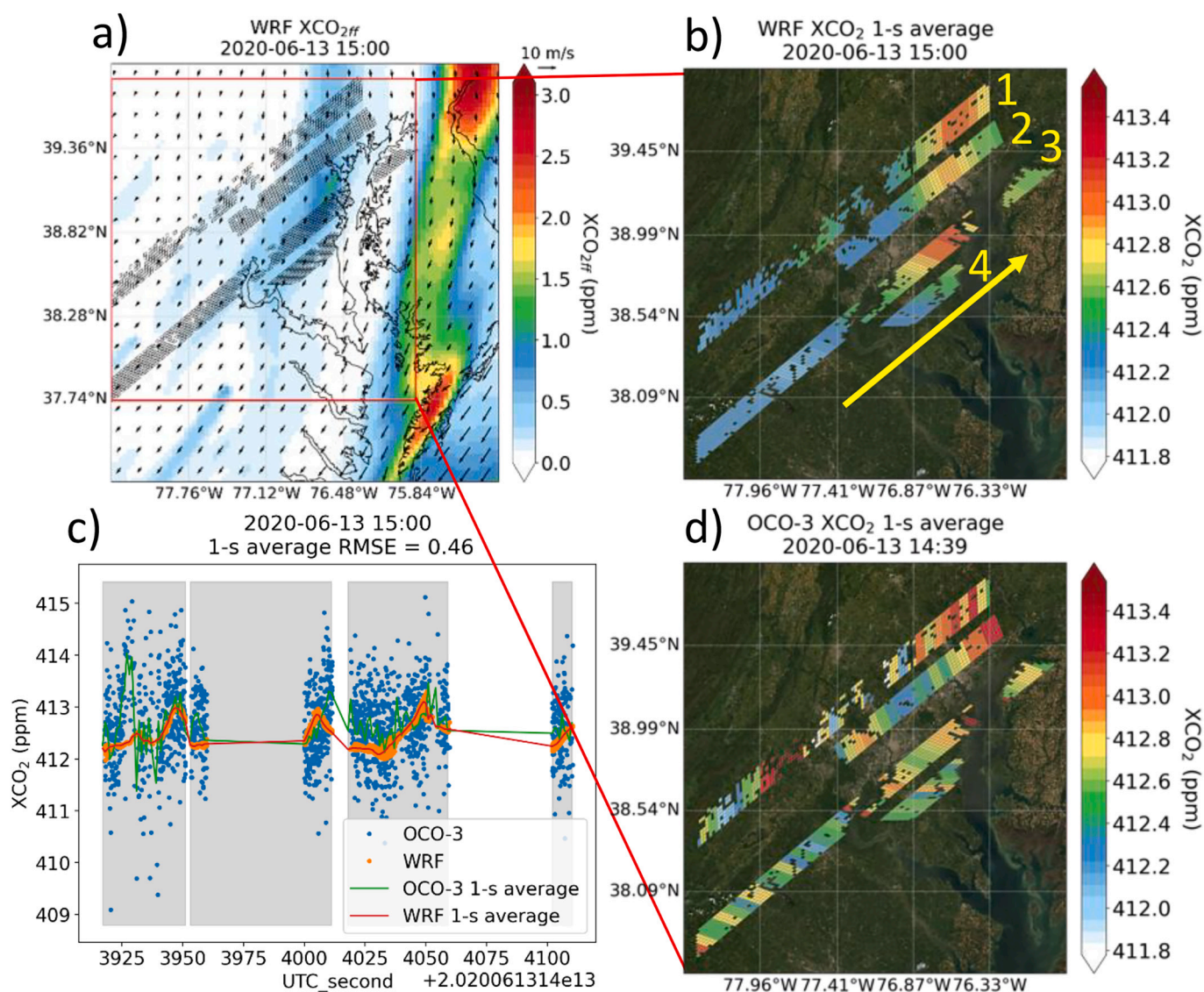


**Fig. 3.** A sample of comparison between XCO<sub>2</sub> from WRF-Chem and OCO-3 over DC-Balt on 2020-06-13 (YYYY-MM-DD): (a) WRF XCO<sub>2ff</sub> at the hour nearest to OCO-3 overpassing time. The black squares represent the locations of OCO-3 pixels. (b) WRF 1-s averaged XCO<sub>2</sub> at OCO-3 pixel locations. The yellow arrow indicates the direction of scanning. The yellow numbers correspond to the order of the different swaths. (c) Time series of XCO<sub>2</sub> following the order of OCO-3 scanning time. The grey boxes in the background represent the time spans of different swaths. WRF XCO<sub>2</sub> is calculated by adding XCO<sub>2bio</sub> based on Biogenic CO<sub>2</sub> fluxes describe in Section 2.3.2, XCO<sub>2ff</sub> in a), and swath background. (d) OCO-3 1-s averaged XCO<sub>2</sub>.

June 2020. Note that the OCO-3 vEarly data contains time-dependent residual pointing errors that occasionally exceed OCO-3's footprint size, especially for large azimuth and elevation positions of the PMA (i. e., swath bias, Taylor et al., 2020), which may still exist in v10r data. Assessment of pointing errors in v10 compared to vEarly suggests that they have been reduced but not removed (O'Dell's presentation at OCO science team meeting in March 2022), although it is difficult to be quantitative for now. Thus, we adjust the background value of WRF-Chem XCO<sub>2</sub> separately for each swath, by minimizing the RMSE between WRF-Chem XCO<sub>2</sub> and OCO-3 XCO<sub>2</sub> for each swath. In the sample case (Fig. 3), a large plume (>1 ppm enhancement) crosses the OCO-3 swaths, simulated by WRF-Chem. But the observed plume originates from the north of the simulation domain (i.e., a power plant near Harrisburg in Pennsylvania) instead of being emitted from within the DC-Balt domain. Another large plume at the eastern edge of the domain, attributed to a power plant near Allentown in Pennsylvania, is not captured by OCO-3 swaths. As reported by Mueller et al. (2018), average ratios of extra urban inflow to total modeled enhancements at urban towers in DC-Balt are 21% to 36% in February and 31% to 43% in July.

Schuh et al. (2021) also found that the signal-to-noise ratios (SNR) of local anthropogenic urban emissions of CO<sub>2</sub> versus the background inflow remains low (0.17 in summer and 0.21 in winter) over New York City, a metropolitan area near DC-Balt.

As for the other two individual cases (Fig. S6 and Fig. S7), WRF-Chem reproduces the XCO<sub>2</sub> gradients observed by OCO-3, though no clear plume from DC-Balt was captured in the OCO-3 SAMs. Over DC-Balt, the lack of detectable  $\Delta$ XCO<sub>2</sub> peaks (i.e., low SNR) in the OCO-3 swaths impairs our ability to perform inversions of the CO<sub>2ff</sub> emissions. However, spatial structures due to distant sources were correctly simulated by WRF-Chem, which confirms the potential of the modeling system to capture urban plumes.

Although the selected cases are of limited use for emission inversion, they demonstrate that WRF-Chem CO<sub>2ff</sub> can be used as a proxy for OCO-3  $\Delta$ XCO<sub>2</sub>. Thus, we compare WRF-Chem XCO<sub>2ff</sub> with TROPOMI NO<sub>2</sub> (Fig. 4, Fig. S6, and Fig. S7) to reconcile the asynchrony of the two satellites. The correlation between NO<sub>2</sub> and XCO<sub>2ff</sub> is low, because the TROPOMI NO<sub>2</sub> does not observe any coherent spatial structures on this day. The low correlation may be caused by the interference of distant

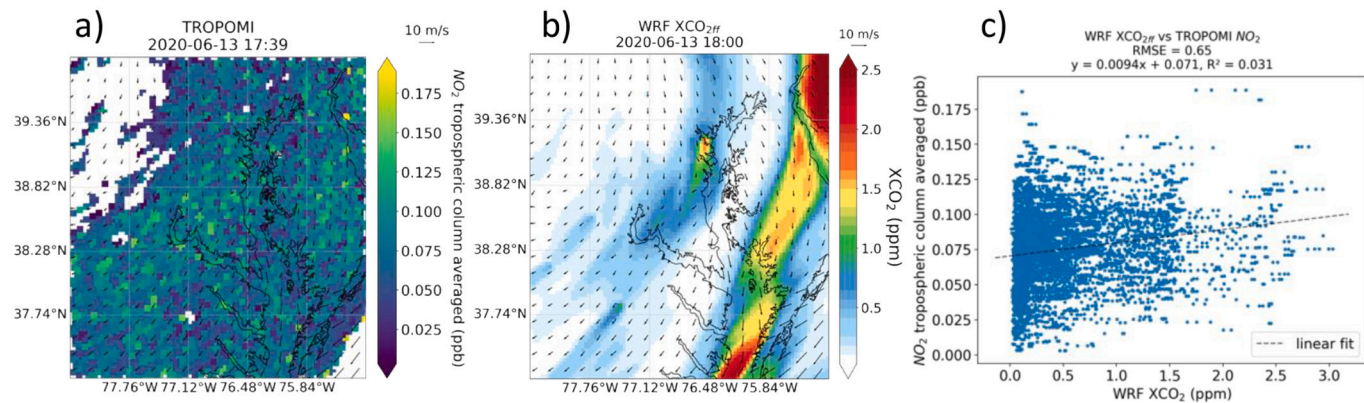


**Fig. 4.** A sample of comparison between TROPOMI NO<sub>2</sub> and WRF-Chem XCO<sub>2diff</sub> over DC-Balt on 2020-06-13 (YYYY-MM-DD): (a) TROPOMI NO<sub>2</sub>; (b) WRF XCO<sub>2diff</sub> at the hour nearest to TROPOMI overpassing time; (c) scatters of TROPOMI NO<sub>2</sub> vs WRF-Chem XCO<sub>2diff</sub>.

sources and the lifetime difference between CO<sub>2</sub> and NO<sub>2</sub>.

We examined six OCO-3 SAMs over Mexico City to evaluate the performance of the WRF-Chem model. Fig. 5 illustrates the comparison

between XCO<sub>2</sub> from WRF-Chem and OCO-3 over Mexico City on March 30, 2020. Additional cases corresponding to the different SAMs are shown in Fig. S8-Fig. S12. Because CO<sub>2</sub> emitted from the urban area

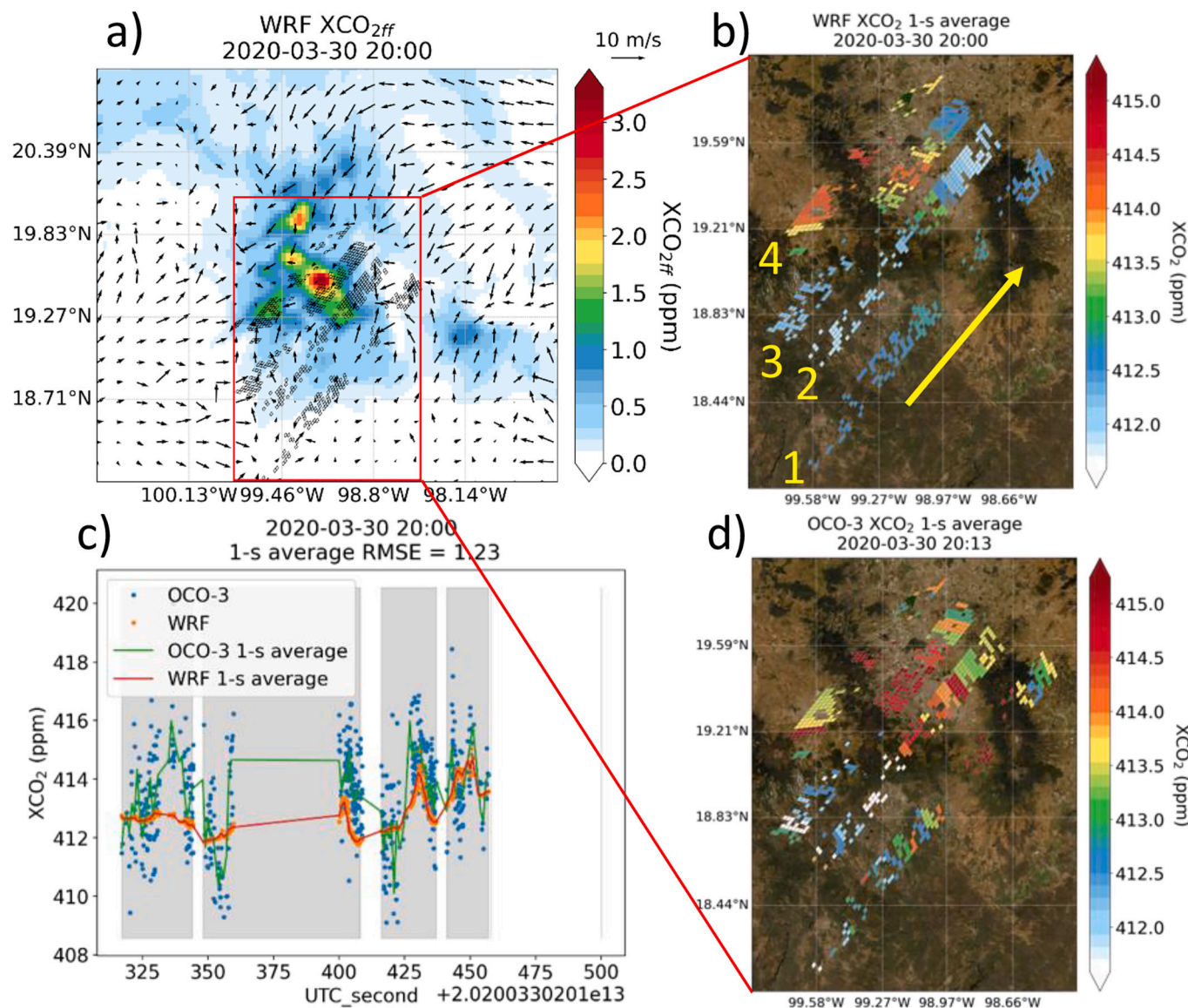


**Fig. 5.** Same as Fig. 3 but for Mexico City on 2020-03-30 (YYYY-MM-DD).

tends to accumulate in the valley (low horizontal wind speed due to the surrounding high topography), WRF-Chem roughly reproduces the position of  $\Delta XCO_{2ff}$  hotspots observed in OCO-3 SAM retrievals. Note that the Mexico City plume from WRF-Chem in Fig. 5a,b looks slightly spatially misplaced relative to OCO-3 SAMs in Fig. 5d, which may be caused by an unrealistic complicated wind pattern in WRF-Chem. A similar plume offset was reported by Zheng et al. (2019).

Fig. 6 illustrates the comparison between TROPOMI  $NO_2$  and WRF-Chem  $XCO_{2ff}$  over Mexico City. Additional cases are shown in Fig. S8-Fig. S12. The positive linear relationship between  $CO_{2ff}$  and  $NO_2$  over Mexico City is larger than over DC-Balt due to the high density of emission sources and the confinement of the urban plume in the valley. The spatial correlation (Fig. 6c) results in a relatively good fit ( $R^2 = 0.57$ ) over the domain. TROPOMI  $NO_2$  retrievals present an enhancement of about 1 ppb in the central part of the domain. Compared to DC-Balt (Fig. 4), despite similar  $XCO_2$  enhancements in WRF-Chem, the modeled mole fractions match the overall  $NO_2$  distribution, possibly due to higher  $NO_2/CO_2$  ratios in Mexico City. We also note that a major enhancement (hotspot) located in the eastern part of the domain (Case March 26, 2020, in Fig. S9) was not reproduced by WRF-Chem, potentially due to the fires detected by MODIS (<https://worldview.earthdata.nasa.gov>).

### 3.2. Reconciliation of the $NO_x$ - $XCO_{2ff}$ mismatch using multiple tracks

For individual cases, the relationship between anthropogenic  $CO_2$  and  $NO_2$  remains unclear, especially for DC-Balt. Therefore, we examined the correlation between  $NO_x$  and  $XCO_2$  using multiple tracks to reduce the noise caused by model transport errors and measurement errors. Due to the limited availability of OCO-3 SAMs, we compared TROPOMI  $NO_2$  with WRF-Chem  $XCO_{2ff}$  over the entire month of February 2020, a cold month before the first wave of the pandemic of COVID-19. We expect a limited impact of the photochemistry and no significant emission reduction (mobility restrictions started in March of 2020) for both cities. Fig. S13 and Fig. S14 show the comparison of single cases in February 2020. On many days, the spatial distributions of  $NO_2$  and  $XCO_{2ff}$  are not collocated, especially over DC-Balt, indicating that the noise from single tracks remains large, consistent with Section 3.1.

Fig. 7a and Fig. 7b show the spatial distribution of both gases when averaging over the entire month over DC-Balt. The hotspots of  $XCO_{2ff}$  and  $NO_2$  over Wilmington in Delaware, Baltimore in Maryland, Washington D.C., and Richmond in Virginia are more clearly co-located after averaging 17 cases for the entire February 2020 compared to individual cases (Fig. S13). We therefore investigated the detectability of homology as a function of the number of cases (both in time and space). To examine the spatial correlations, we averaged  $XCO_{2ff}$  and  $NO_2$  maps in  $n$  cases following the time sequence (referred as  $n$ -case averaging time window) to get  $N + 1 - n$  pairs of averaged maps, where  $N$  is the total

number of TROPOMI  $NO_2$  cases ( $N = 17$  for DC-Balt, and  $N = 16$  for Mexico City;  $1 \leq n \leq N$ ) in February 2020. Then for each  $XCO_{2ff}$ - $NO_2$  pair of maps, we calculated the  $R^2$  (referred as spatial  $R^2$ ,  $R_s^2$ ) and slope of the linear fit of all pixels of  $NO_2/XCO_{2ff}$  (referred as spatial ratio,  $r_s$ ). Fig. 7c shows  $R_s^2$  as a function of the number of cases ( $n$ ) ( $r_s$  as a function of  $n$  is shown in Fig. 7e).

To calculate the temporal correlation of  $NO_2$  and  $XCO_{2ff}$ , we firstly averaged  $N + 1 - n$  pairs of  $NO_2$  and  $XCO_{2ff}$  maps (each map is an average of  $n$  days). For each  $XCO_{2ff}$ - $NO_2$  pair of maps, we calculated the means of the  $NO_2$  and  $XCO_{2ff}$ . Then we calculated the  $R^2$  (referred as temporal  $R^2$ ,  $R_t^2$  in Fig. 7d) and slope (referred as temporal ratio,  $r_t$  in Fig. 7f) of the linear fit of the  $N + 1 - n$   $XCO_{2ff}$ - $NO_2$  pairs of means of  $NO_2$  and  $XCO_{2ff}$ . We only show the relationship where  $n$  is not greater than eight because the sample size (i.e.,  $N + 1 - n$  pairs) is too small to represent the temporal relationship between  $XCO_{2ff}$  and  $NO_2$  over DC-Balt when  $n > 8$ .

Both the  $R_t^2$  and  $r_t$  increase as the number of images (days) increase, then eventually flatten when the number of images (days) within the time window is  $>12$ . This result implies that the noise interferences in  $NO_2$  images and the impact of distant sources in  $CO_2$  images can be partially removed by multitrack averaging using up to 12 images, while using  $>12$  images would not be helpful to further remove the interferences. The  $R_t^2$  increases from 0.5 to 0.9 when increasing the length of the averaging time window from one to eight, indicating that temporal variations of  $XCO_{2ff}$  may be better traced by the variations in  $NO_2$  using longer temporal averages. Given 17 images available in a month, we may trace the 20-day moving average of  $CO_{2ff}$  emissions using  $NO_2$  as a proxy.

Fig. 8 shows the results of multitrack averaging over Mexico City. Like DC-Balt, the  $R_s^2$  and  $r_s$  both increase with the length of our averaging time window, then flatten when the window length is greater than ten. The averaged  $r_s$  over DC-Balt is much lower than Mexico City, indicating a better control of  $NO_2$  emissions in DC-Balt resulting from stricter emission restrictions and a more efficient vehicle fleet. Also, the higher altitude of Mexico City affects the combustion efficiency and thus produces more  $NO_2$ . The  $R_s^2$  over Mexico City is much greater than DC-Balt due to the valley trapping phenomenon, which is consistent with our individual case comparison. The  $R_t^2$  of the whole domain (blue line in Fig. 8d) is significantly smaller than DC-Balt, potentially due to the intermittent wildfires near Mexico City during February 2020 detected by MODIS. We tried to screen the effects of fires by applying a mask (average  $XCO_{2ff} > 0.5$  ppm), covering the valley of Mexico City (Fig. 8ab). The  $R_t^2$  with the mask (orange line in Fig. 8d) is higher than without the mask but still smaller than over DC-Balt. It indicates that the fire is the main obstacle of tracking temporal  $CO_{2ff}$  variations using  $NO_2$  but can be partially screened by the high  $CO_{2ff}$  area mask.

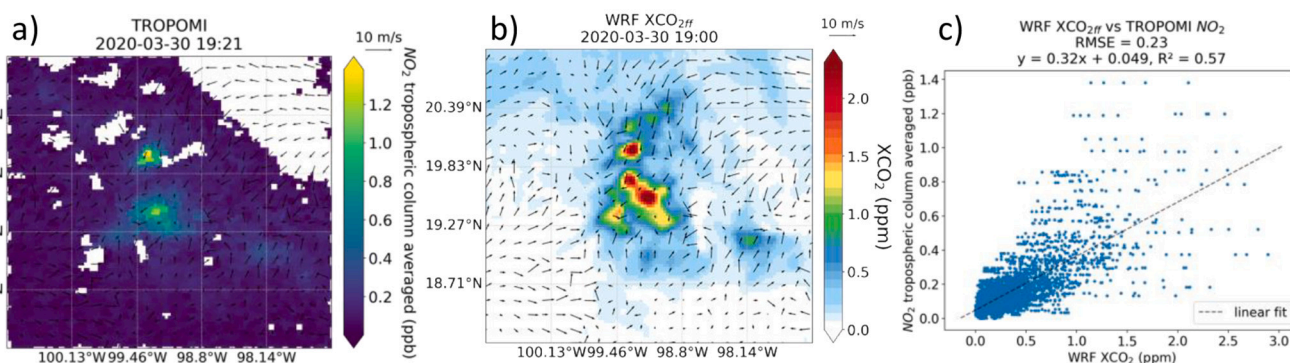
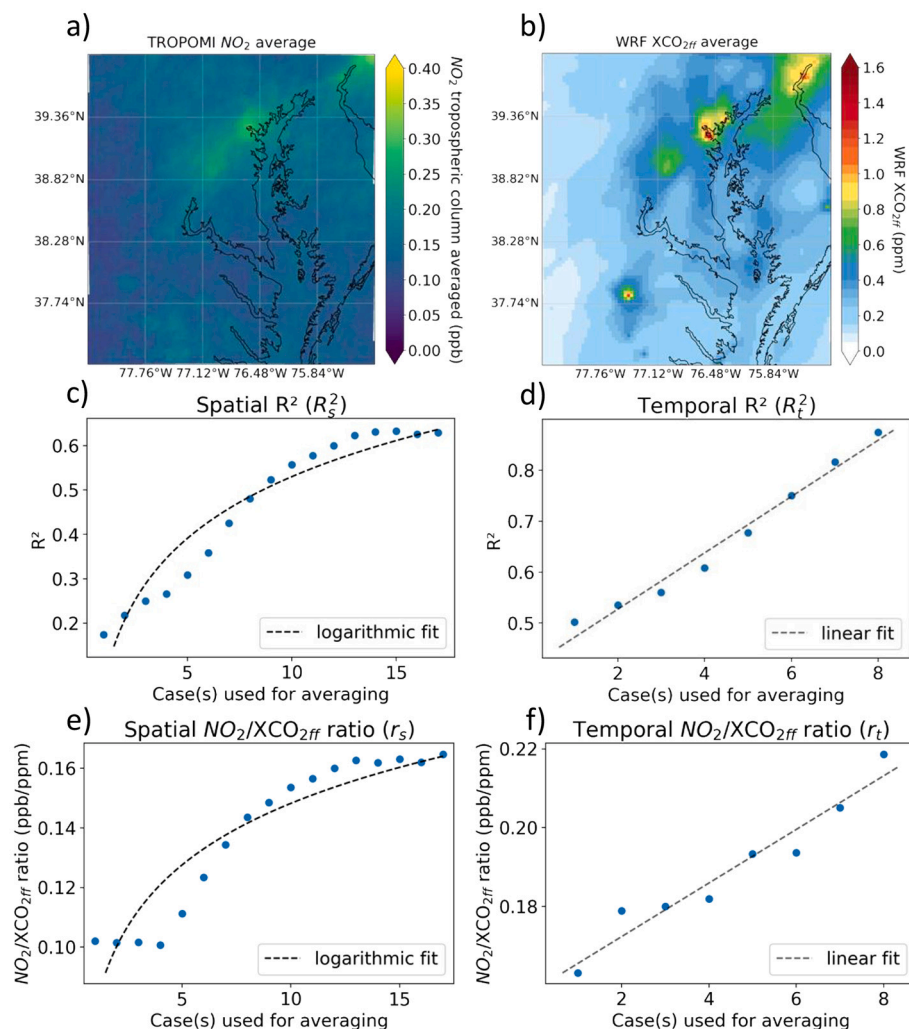


Fig. 6. Same as Fig. 4 but for Mexico City on 2020-03-30 (YYYY-MM-DD).



**Fig. 7.** 1-month multitrack averaging of  $XCO_{2ff}$  vs  $NO_2$  over DC-Balt: (a) all-case averaged TROPOMI  $NO_2$ ; (b) all-case averaged WRF  $XCO_{2ff}$ ; (c) spatial correlation coefficient ( $R_s^2$ ) vs the number of cases used for multi-track averaging; (d) same as (c) but for temporal correlation coefficient ( $R_t^2$ ); (e) spatial  $NO_2$ :  $XCO_{2ff}$  ratio ( $r_s$ ) vs. the number of cases used for multi-track averaging; (f) same as (d) but for temporal ratio ( $r_t$ ). The case(s) in (c–f) means the number of valid TROPOMI frames used for averaging.

#### 4. Discussion

We use WRF-Chem output as a proxy between overpassing times of OCO-3 SAMs and TROPOMI, but also as a tool to explore current limitations in the scanning mode for urban areas. The first limitation is related to the spatial coverage of OCO-3 SAMs. With only a few swaths over a city target, OCO-3 SAM coverage is much smaller than TROPOMI and often excludes a fraction of the surroundings or even a fraction of the city plume itself. Because of the limited coverage, the characterization of background conditions remains highly uncertain, as observed over DC-Balt when sampling  $CO_2$  enhancements emitted by distant sources. Metropolitan areas surrounded by other cities or by large point sources are affected by spatial structures in the background, possibly leading to a false interpretation of long-distance plumes observed in SAMs. This limitation can be addressed with regional models including non-local sources but will remain challenging for integrated mass enhancement approaches (Kuhlmann et al., 2020). The model accuracy also is affected by challenging conditions of high wind speeds (during which enhancements are less clear due to mixing and ventilation) or challenging conditions of very low wind speeds (in which the relative wind speed uncertainties tend to be high, making accurate emission estimation difficult).

Our analysis of WRF-Chem simulations showed that spatial structures can vary significantly between  $XCO_{2ff}$  and  $NO_2$ . Correlation decreases further when considering the time lag due to the overpassing times of OCO-3 and TROPOMI. Until synchronized retrievals become

available (e.g., the CO2M mission; Bézy et al., 2019), transport models will be required to bridge the temporal gap. In addition, variations in sectoral emissions further complicate the  $NO_2/CO_2$  ratios, which needs to be addressed in multi-species inventories. Overall, despite the sampling differences in time and space, some information relative to fossil fuel emissions can be recovered when averaging over multiple cases.

The in situ evaluation of WRF-Chem  $CO_2$  outputs shows that WRF-Chem can reproduce hourly variation in near-surface  $CO_2$  enhancements during afternoon (Fig. 2 and Fig. S1). It suggests that tower-based networks observing larger enhancements than satellite retrievals can be used to measure shorter temporal variations in emissions. We notice that the linear relationship is even more visible when aggregating measurements from the 13 tower sites (afternoon hours only) over DC-Balt, indicating the multi-case averaging is not only helpful for satellite-based measurements but also in situ data.

While  $NO_x/CO_{2ff}$  emission ratios have been recently studied and quantified, TROPOMI only observes  $NO_2$ . A fixed 1.33 (Goldberg et al., 2019b, 2019a) or pre-calculated  $NO_x/NO_2$  ratios (Lorente et al., 2019; Zheng et al., 2020) has usually been adopted by previous studies when quantifying  $NO_x$  emissions based on satellite data. But diurnal and seasonal variations in the  $NO_x/NO_2$  ratio due to emission sources and chemistry should be taken into consideration, especially in studies aiming to resolve weekly temporal scales. In this study, we only focused on short-term emission variations assuming that our  $NO_x/CO_{2ff}$  emission ratio remains constant. But sectoral differences may also affect  $NO_x/CO_{2ff}$  emission ratios over time, which adds a significant unknown to the

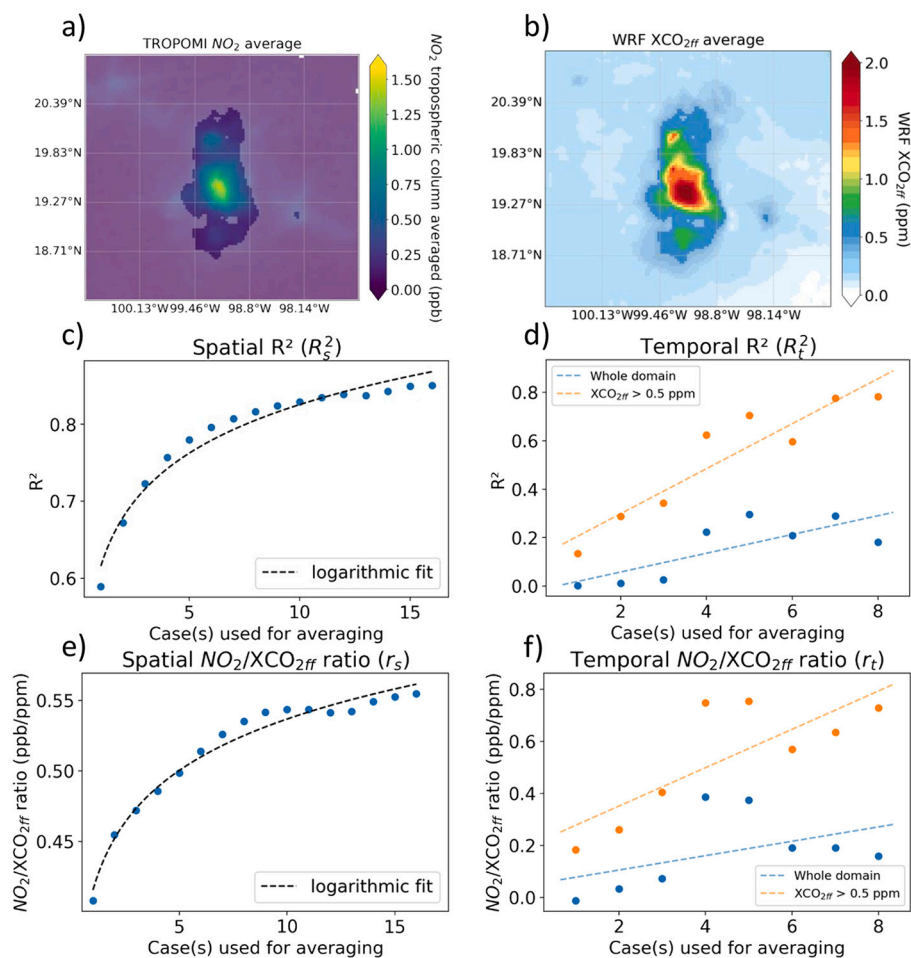


**Fig. 8.** Same as Fig. 7 but for Mexico City. Note: the areas with average XCO<sub>2ff</sub> ≤ 0.5 ppm are shaded by translucent masks in (a) and (b). (d) shows temporal correlation coefficient (R<sub>t</sub><sup>2</sup>) in the whole domain and the areas within the area with average XCO<sub>2ff</sub> > 0.5 ppm; (f) same as (d) but for temporal ratio (r<sub>t</sub>).

inverse problem (Zheng et al., 2020). We adjusted sectoral CO<sub>2ff</sub> emissions in WRF-Chem inputs based on NO<sub>x</sub>/CO<sub>2ff</sub> emission ratios from CAMS, EDGAR, and NEI but failed to improve the spatial correlation between NO<sub>2</sub> and CO<sub>2ff</sub>. Further investigation on sectoral differences is needed to simulate both NO<sub>2</sub> and CO<sub>2</sub> mole fractions within a joint modeling system.

The spatial correlation coefficient (R<sub>s</sub><sup>2</sup>) of Mexico City is higher than DC-Balt, while the temporal correlation coefficient (R<sub>t</sub><sup>2</sup>) of Mexico City remains smaller. This discrepancy reveals the subtle differences in fossil fuel estimations depending on the city landscape. Because DC-Balt has a flat topography, similar to New York as reported by Schuh et al. (2021), in addition to potential interferences from nearby cities, it is difficult to quantify the CO<sub>2ff</sub> emissions based on individual cases. But multitrack averaging reconciles most of the spatial mismatches. As for Mexico City, the infrequent influence of nearby sources and the surrounding mountains isolate and trap the CO<sub>2ff</sub> in the valley, resulting in high spatial correlations when trying to quantify CO<sub>2ff</sub> emissions based on individual cases (median difficulty reported by Schuh et al., 2021). But potential biases in inverse emissions over Mexico City could be large over time, primarily caused by the intermittent wildfires. The bias in ventilation rate (overestimates by 3.37 m/s at heights below 700 hPa, Fig. S5c) could be another reason for small R<sub>t</sub><sup>2</sup> over Mexico City. Effective methods for screening the effects of fires and improving the accuracy of the simulated ventilation rate are needed to better track day-to-day changes in CO<sub>2ff</sub> emissions over Mexico City.

## 5. Conclusions

In this study, we reconciled the asynchronous TROPOMI NO<sub>2</sub> and OCO-3 ΔXCO<sub>2</sub> SAMs with WRF-Chem over a multicity region, DC-Balt, and a basin city, Mexico City, for single and multiple tracks. DC-Balt and Mexico City show different challenges in explaining the relationship between NO<sub>2</sub> and CO<sub>2ff</sub> due to different topography and distant emissions.

As a validation of the modeling system, we showed the model successfully simulates afternoon hourly variations of CO<sub>2</sub> enhancements observed by in situ sites for both cities. For DC-Balt, WRF-Chem captures the ΔXCO<sub>2</sub> when a plume crosses the OCO-3 tracks. We also noted technical difficulties to invert CO<sub>2ff</sub> emissions for DC-Balt because the detected plume originates from other cities (i.e., Harrisburg, Pennsylvania and New York City, New York) instead of DC-Balt. For Mexico City, the surrounding mountains trap the NO<sub>2</sub> and CO<sub>2</sub> in the valley, reinforcing the apparent spatial correlations between WRF-Chem and satellite images (XCO<sub>2</sub> and TROPOMI), clearer than DC-Balt. One hot-spot of NO<sub>2</sub> at the east of Mexico City was still missing in WRF-Chem, which might be caused by the nearby wildfires.

Due to the limited availability of OCO-3 SAMs, we tested how multitrack averaging helps reconcile the mismatch between NO<sub>2</sub> and CO<sub>2ff</sub> by comparing TROPOMI data and WRF-Chem outputs in February 2020. R<sub>s</sub><sup>2</sup> and r<sub>s</sub> reached maximum values when averaging >12 continuous images for DC-Balt and >10 continuous images for Mexico City, indicating that multitrack averaging helps eliminate distant interferences. It also implies that tracking the 20-day moving average of

CO<sub>2ff</sub> emissions using TROPOMI NO<sub>2</sub> is technically feasible considering available TROPOMI cases (17 cases over DC-Balt and 16 cases over Mexico City) in our selected month. NO<sub>2</sub>/CO<sub>2ff</sub> ratios over DC-Balt are smaller than Mexico City, indicative of stricter emission restrictions, a more efficient vehicle fleet, and higher combustion efficiency due to lower altitude in DC-Balt.  $R_t^2$  over Mexico City is smaller than DC-Balt, which can be partially improved by screening the effects of intermittent fires near Mexico City using a mask of high CO<sub>2ff</sub> areas. The large model transport errors (esp. wind speed) in the Mexico City basin could be another reason for the small  $R_t^2$ .

In summary, multitrack averaging using modeled CO<sub>2ff</sub> as a proxy is helpful to filter the noise in single-track images, to cancel the interference from distant sources, and to magnify correlations between NO<sub>2</sub> and CO<sub>2ff</sub>. A basin city like Mexico City has stronger spatial correlations but weaker temporal correlations than a multicity region like DC-Balt due to intermittent fires and large transport errors caused by the trapping effects of the surrounding mountains. Tracking 20-day moving average of CO<sub>2ff</sub> emissions using TROPOMI NO<sub>2</sub> seems technically feasible, considering the relationship between correlation coefficients and the number of available images. Further work remains to be done to convert correlations between satellite-based NO<sub>2</sub> and ΔXCO<sub>2</sub> to correlations of fossil fuel emissions, including building dynamic NO<sub>x</sub>/NO<sub>2</sub> ratios, improving the method of extracting fossil fuel signals (urban plumes) from satellite images, and minimizing the model transport errors over basin cities.

#### Data availability

The following data in this study is available from public sources:  
 NCAR Upper Air Database: [https://rda.ucar.edu/datasets/ds370.1/OCO-3\\_L2\\_Lite\\_v10r\\_CO2/](https://rda.ucar.edu/datasets/ds370.1/OCO-3_L2_Lite_v10r_CO2/)  
 CO<sub>2</sub>: <https://disc.gsfc.nasa.gov/datasets?key words=oco-3%2010r&page=1>  
 TROPOMI NO<sub>2</sub>: <http://www.tropomi.eu/data-products/data-access>  
 ERA5 climate reanalysis: <https://climate.copernicus.eu/climate-reanalysis>  
 CAMS global emissions: <https://ads.atmosphere.copernicus.eu/cdsapp#!/dataset/cams-global-emission-inventories?tab=form>  
 Vulcan Fossil Fuel CO<sub>2</sub> Emissions: [https://daac.ornl.gov/NACP/guides/Vulcan\\_V3\\_Annual\\_Emissions.html](https://daac.ornl.gov/NACP/guides/Vulcan_V3_Annual_Emissions.html)  
 North-East Corridor Baltimore/Washington Project CO<sub>2</sub> data: <https://www.nist.gov/topics/northeast-corridor-urban-test-bed/data>  
 UNAM tower data: <https://www.ruoa.unam.mx/>  
 UNAM emission: [https://github.com/JoseAgustin/emis\\_2016](https://github.com/JoseAgustin/emis_2016)  
 VPRM: <https://data.nist.gov/od/id/mds2-2382>  
 Gridded Ensembles of Surface Biogenic Carbon Fluxes: [https://daac.ornl.gov/cgi-bin/dsvviewer.pl?ds\\_id=1675](https://daac.ornl.gov/cgi-bin/dsvviewer.pl?ds_id=1675)  
 CAMS-GLOB-ANT V4.2: <https://ads.atmosphere.copernicus.eu/cdsapp#!/dataset/cams-global-emission-inventories?tab=overview>

#### CRedit authorship contribution statement

**Ruixue Lei:** Writing – original draft, Methodology, Investigation, Visualization. **Sha Feng:** Conceptualization, Supervision, Methodology, Writing – review & editing. **Yang Xu:** Data curation. **Sophie Tran:** Data curation. **Michel Ramonet:** Writing – review & editing. **Michel Grutter:** Writing – review & editing. **Agustin Garcia:** Data curation, Writing – review & editing. **Mixtli Campos-Pineda:** Writing – review & editing. **Thomas Lauvaux:** Conceptualization, Supervision, Methodology, Writing – review & editing.

#### Declaration of Competing Interest

The authors declare that they have no known competing financial interests or personal relationships that could have appeared to influence the work reported in this paper.

#### Acknowledgments

This work has been funded jointly by the NASA grants #80NSSC18K1313 (subcontracted from the Universities Space Research Association #05783-01 to Penn State) and #80NSSC19k0093. S. Feng is also supported by NASA grant #80HQTR21T0070 at Pacific Northwest National Laboratory (PNNL). PNNL is operated for the Department of Energy by Battelle Memorial Institute under contract DE-AC06-76RL01830. T. Lauvaux has been supported by the French research program Make Our Planet Great Again (Project CIUDAD).

Financial support for measurements in Mexico-City came from the CONACYT-ANR project 290589 ‘Mexico City’s Regional Carbon Impacts – MERCI-CO<sub>2</sub>’ (ANR-17-CE04-0013-01). The RUOA network (Red Universitaria de Observatorios Atmosféricos) operated by UNAM is acknowledged for providing the data. M. Campos-Pineda was funded by DGAPA-UNAM.

Computing resources supporting this work were provided by the NASA High-End Computing (HEC) Program through the NASA Advanced Supercomputing (NAS) Division at Ames Research Center.

We also thank Anna Karion, Sharon Gourdji, and Kim Mueller at National Institute of Standards and Technology for the guidance on using CO<sub>2</sub> measurements in the North-East Corridor Baltimore/Washington Project and Andrew Pitman (PNNL) for editing this manuscript.

#### Appendix A. Supplementary data

Supplementary data to this article can be found online at <https://doi.org/10.1016/j.rse.2022.113241>.

#### References

- Ammoura, L., Xueref-Remy, I., Gros, V., Baudic, A., Bonsang, B., Petit, J.-E., Perrussel, O., Bonnaire, N., Sciare, J., Chevallier, F., 2014. Atmospheric measurements of ratios between CO<sub>2</sub> and co-emitted species from traffic: a tunnel study in the Paris megacity. *Atmos. Chem. Phys.* 14, 12871–12882. <https://doi.org/10.5194/acp-14-12871-2014>.
- Andres, R.J., Boden, T.A., Higdon, D., 2014. A new evaluation of the uncertainty associated with CDIAC estimates of fossil fuel carbon dioxide emission. *Tellus B: Chem. Phys. Meteorol.* 66, 23616. <https://doi.org/10.3402/tellusb.v66.23616>.
- Atkinson, R., 2000. Atmospheric chemistry of VOCs and NO<sub>x</sub>. *Atmos. Environ.* 34, 2063–2101. [https://doi.org/10.1016/S1352-2310\(99\)00460-4](https://doi.org/10.1016/S1352-2310(99)00460-4).
- Beirle, S., Borger, C., Dörner, S., Eskes, H., Kumar, V., de Laat, A., Wagner, T., 2021. Catalog of NO<sub>x</sub> emissions from point sources as derived from the divergence of the NO<sub>2</sub> flux for TROPOMI. *Earth Syst. Sci. Data* 13, 2995–3012. <https://doi.org/10.5194/essd-13-2995-2021>.
- Berezin, E.V., Kononov, I.B., Ciaï, S., Richter, A., Tao, S., Janssens-Maenhout, G., Beekmann, M., Schulze, E.-D., 2013. Multiannual changes of CO<sub>2</sub> emissions in China: indirect estimates derived from satellite measurements of tropospheric NO<sub>2</sub> columns. *Atmos. Chem. Phys.* 13, 9415–9438. <https://doi.org/10.5194/acp-13-9415-2013>.
- Bézy, J.-L., Sierk, B., Löscher, A., Meijer, Y., Nett, H., Fernandez, V., 2019. The European Copernicus Anthropogenic CO<sub>2</sub> Monitoring Mission. In: *IGARSS 2019 - 2019 IEEE International Geoscience and Remote Sensing Symposium*, pp. 8400–8403. <https://doi.org/10.1109/IGARSS.2019.8899116>.
- Birof, F., 2008. In: *World Energy Outlook, 23. International Energy Agency, Paris*, p. 329.
- del Castillo, E.G., Taquet, N., Bezanilla, A., Stremme, W., Ramonet, M., Laurent, O., Xu, Y., Delmotte, M., Grutter, M., 2020. CO<sub>2</sub> variability in the Mexico City region from in situ measurements at an urban and a background site. *Atmosfera* 5 (2), 377–393. <https://doi.org/10.20937/atm.52956>.
- Chavez-Baeza, C., Sheinbaum-Pardo, C., 2014. Sustainable passenger road transport scenarios to reduce fuel consumption, air pollutants and GHG (greenhouse gas) emissions in the Mexico City metropolitan area. *Energy* 66, 624–634.
- Crippa, M., Oreggioni, G., Muntean, M., Schaaf, E., Lo Vullo, E., Solazzo, E., Monforti, F., Oliver, J., Vignati, E., 2019. Fossil CO<sub>2</sub> and GHG Emissions of All World Countries. Publications Office of the European Union, Luxembourg. <https://doi.org/10.2760/687800>.
- Crippa, M., Guizzardi, D., Muntean, M., Schaaf, E., Solazzo, E., Monforti-Ferrario, F., Olivier, J., Vignati, E., 2020. Fossil CO<sub>2</sub> Emissions of All World Countries: 2020 Report.
- Crowell, S., Baker, D., Jacobson, A.R., Basu, S., Liu, J., Schuh, A.E., Chevallier, F., Deng, F., Feng, L., Chatterjee, A., 2019. Improved Regional CO<sub>2</sub> Flux Estimates from OCO-2 v9 Retrievals. *AGU Fall Meeting Abstracts*, 52.
- Dong, H., Dai, H., Dong, L., Fujita, T., Geng, Y., Klimont, Z., Inoue, T., Bunya, S., Fujii, M., Masui, T., 2015. Pursuing air pollutant co-benefits of CO<sub>2</sub> mitigation in China: a provincial level analysis. *Appl. Energy* 144, 165–174. <https://doi.org/10.1016/j.apenergy.2015.02.020>.

- Dou, X., Wang, Y., Clais, P., Chevallier, F., Davis, S.J., Crippa, M., Janssens-Maenhout, G., Guizzardi, D., Solazzo, E., Yan, F., Huo, D., Bo, Z., Deng, Z., Zhu, B., Wang, H., Zhang, Q., Gentine, P., Liu, Z., 2021. Global Gridded Daily CO<sub>2</sub> 25 Emissions arXiv:2107.08586 [physics, q-fin].
- Dou, X., Wang, Y., Clais, P., Chevallier, F., Davis, S.J., Crippa, M., Janssens-Maenhout, G., Guizzardi, D., Solazzo, E., Yan, F., Huo, D., Bo, Z., Zhu, B., Cui, D., Ke, P., Sun, T., Wang, H., Zhang, Q., Gentine, P., Deng, Z., Liu, Z., 2021b. Near-real-time global gridded daily CO<sub>2</sub> emissions. *Innovation* 100182. <https://doi.org/10.1016/j.xinn.2021.100182>.
- Eldering, A., Taylor, T.E., O'Dell, C.W., Pavlick, R., 2019. The OCO-3 mission: measurement objectives and expected performance based on 1 year of simulated data. *Atmos.Meas.Tech.* 12, 2341–2370. <https://doi.org/10.5194/amt-12-2341-2019>.
- van Geffen, J., Eskes, H., Compennolle, S., Pinardi, G., Verhoelst, T., Lambert, J.-C., Sneep, M., ter Linden, M., Ludewig, A., Boersma, K.F., Veeffkind, J.P., 2022. Sentinel-5P TROPOMI NO<sub>2</sub> retrieval: impact of version v2.2 improvements and comparisons with OMI and ground-based data. *Atmos.Meas.Tech.* 15, 2037–2060. <https://doi.org/10.5194/amt-15-2037-2022>.
- Goldberg, D.L., Lu, Z., Streets, D.G., de Foy, B., Griffin, D., McLinden, C.A., Lamsal, L.N., Krotkov, N.A., Eskes, H., 2019a. Enhanced capabilities of TROPOMI NO<sub>2</sub>: estimating NOX from North American cities and power plants. *Environ. Sci. Technol.* 53, 12594–12601. <https://doi.org/10.1021/acs.est.9b04488>.
- Goldberg, D.L., Saide, P.E., Lamsal, L.N., De Foy, B., Lu, Z., Woo, J.-H., Kim, Y., Kim, J., Gao, M., Carmichael, G., 2019b. A top-down assessment using OMI NO<sub>2</sub> suggests an underestimate in the NO<sub>x</sub> emissions inventory in Seoul, South Korea, during KORUS-AQ. *Atmos.Chem.Phys.* 19.
- Goldberg, D.L., Anenberg, S.C., Kerr, G.H., Mohegh, A., Lu, Z., Streets, D.G., 2021. TROPOMI NO<sub>2</sub> in the United States: a detailed look at the annual averages, weekly cycles, effects of temperature, and correlation with surface NO<sub>2</sub> concentrations. *Earth's Future* 9, e2020EF001665. <https://doi.org/10.1029/2020EF001665>.
- Gourdji, S., Karion, A., Lopez-Coto, I., Ghosh, S., Mueller, K.L., Zhou, Y., Williams, C.A., Baker, I.T., Haynes, K., Whetstone, J., 2021. A modified vegetation photosynthesis and respiration model (VPRM) for the eastern USA and Canada, evaluated with comparison to atmospheric observations and other biospheric models [WWW Document]. *Earth Space Sci.Open Arch.* <https://doi.org/10.1002/essoar.10506768.1>.
- Grell, A., Peckham, E., Schmitz, R., McKeen, A., Frost, G., Skamarock, W., Eder, B., 2005. Fully-coupled online chemistry within the WRF model. *Atmos. Environ.* 6957–6975. <https://doi.org/10.1016/j.atmosenv.2005.04.027>.
- Gurney, K., Liang, J., Zhou, Y., Benes, B., Patarasuk, R., 2018. Hestia Fossil Fuel Carbon Dioxide Emissions Inventory for Urban Regions. <https://doi.org/10.18434/T4/1502499>.
- Gurney, K.R., Liang, J., Patarasuk, R., Song, Y., Huang, J., Roest, G., 2019. Vulcan: High-Resolution Annual Fossil Fuel CO<sub>2</sub> Emissions in USA, 2010–2015, Version 3. ORNL DAAC. <https://doi.org/10.3334/ORNLDAAC/1741>.
- Hakkara, J., Szelag, M.E., Jalongo, I., Retscher, C., Oda, T., Crisp, D., 2021. Analyzing nitrogen oxides to carbon dioxide emission ratios from space: a case study of Matimba Power Station in South Africa. *Atmos.Environ.* 10, 100110. <https://doi.org/10.1016/j.aeoa.2021.100110>.
- Hersbach, H., Bell, B., Berrisford, P., Hirahara, S., Horányi, A., Muñoz-Sabater, J., Nicolas, J., Peubey, C., Radu, R., Schepers, D., Simmons, A., Soci, C., Abdalla, S., Abellan, X., Balsamo, G., Bechtold, P., Biavati, G., Bonville, J., Bonville, M., Chiara, G. D., Dahlgren, P., Dee, D., Diamantakis, M., Dragani, R., Flemming, J., Forbes, R., Fuentes, M., Geer, A., Haimberger, L., Healy, S., Hogan, R.J., Hólm, E., Janisková, M., Keeley, S., Laloyaux, P., Lopez, P., Lupu, C., Radnoti, G., de Rosnay, P., Rozum, I., Vamborg, F., Villaume, S., Thépaut, J.-N., 2020. The ERA5 global reanalysis. *Q. J. R. Meteorol. Soc.* 146, 1999–2049. <https://doi.org/10.1002/qj.3803>.
- IPCC, 2014. AR5 Synthesis Report: Climate Change.
- Judd, L.M., Al-Saadi, J.A., Szykman, J.J., Valin, L.C., Janz, S.J., Kowalewski, M.G., Eskes, H.J., Veeffkind, J.P., Cede, A., Mueller, M., Gebetsberger, M., Swap, R., Pierce, R.B., Nowlan, C.R., Abad, G.G., Nehrir, A., Williams, D., 2020. Evaluating sentinel-5P TROPOMI tropospheric NO<sub>2</sub> column densities with airborne and Pandora spectrometers near New York City and Long Island Sound. *Atmos.Meas.Tech.* 13, 6113–6140. <https://doi.org/10.5194/amt-13-6113-2020>.
- Karion, A., Callahan, W., Stock, M., Prinziavalli, S., Verhulst, K.R., Kim, J., Salameh, P.K., Lopez-Coto, I., Whetstone, J., 2020. Greenhouse gas observations from the Northeast Corridor tower network. *Earth Syst.Sci.Data* 12, 699–717. <https://doi.org/10.5194/essd-12-699-2020>.
- Kiel, M., Eldering, A., Roten, D.D., Lin, J.C., Feng, S., Lei, R., Lauvaux, T., Oda, T., Roehl, C.M., Blavier, J.-F., Iraci, L.T., 2021. Urban-focused satellite CO<sub>2</sub> observations from the Orbiting Carbon Observatory-3: a first look at the Los Angeles megacity. *Remote Sens. Environ.* 258, 112314. <https://doi.org/10.1016/j.rse.2021.112314>.
- Kuhlmann, G., Broquet, G., Marshall, J., Clément, V., Löscher, A., Meijer, Y., Brunner, D., 2019. Detectability of CO<sub>2</sub> emission plumes of cities and power plants with the Copernicus Anthropogenic CO<sub>2</sub> Monitoring (CO<sub>2</sub>M) mission. *Atmos.Meas.Tech.* 12, 6695–6719. <https://doi.org/10.5194/amt-12-6695-2019>.
- Kuhlmann, G., Brunner, D., Broquet, G., Meijer, Y., 2020. Quantifying CO<sub>2</sub> Emissions of a City With the Copernicus Anthropogenic CO<sub>2</sub> Monitoring Satellite Mission, 33.
- Lauvaux, T., Schuh, A.E., Ullrich, M., Richardson, S., Miles, N., Andrews, A.E., Sweeney, C., Diaz, L.I., Martins, D., Shepson, P.B., Davis, K.J., 2012. Constraining the CO<sub>2</sub> budget of the corn belt: exploring uncertainties from the assumptions in a mesoscale inverse system. *Atmos. Chem. Phys.* 12, 337–354. <https://doi.org/10.5194/acp-12-337-2012>.
- Lei, R., Feng, S., Danjou, A., Broquet, G., Wu, D., Lin, J.C., O'Dell, C.W., Lauvaux, T., 2021. Fossil fuel CO<sub>2</sub> emissions over metropolitan areas from space: a multi-model analysis of OCO-2 data over Lahore, Pakistan. *Remote Sens. Environ.* 264, 112625. <https://doi.org/10.1016/j.rse.2021.112625>.
- Li, M., Zhang, Q., Kurokawa, J., Woo, J.-H., He, K., Lu, Z., Ohara, T., Song, Y., Streets, D. G., Carmichael, G.R., 2017. MIX: a mosaic Asian anthropogenic emission inventory under the international collaboration framework of the MICS-Asia and HTAP. *Atmos. Chem.Phys.* 17.
- Liu, Z., Clais, P., Deng, Z., Davis, S.J., Zheng, B., Wang, Y., Cui, D., Zhu, B., Dou, X., Ke, P., Sun, T., Guo, Rui, Zhong, H., Boucher, O., Bréon, F.-M., Lu, C., Guo, Runtao, Xue, J., Boucher, E., Tanaka, K., Chevallier, F., 2020a. Carbon monitor, a near-real-time daily dataset of global CO<sub>2</sub> emission from fossil fuel and cement production. *Sci. Data* 7, 392. <https://doi.org/10.1038/s41597-020-00708-7>.
- Liu, Z., Clais, P., Deng, Z., Lei, R., Davis, S.J., Feng, S., Zheng, B., Cui, D., Dou, X., Zhu, B., Guo, Rui, Ke, P., Sun, T., Lu, C., He, P., Wang, Yuan, Yue, X., Wang, Yilong, Lei, Y., Zhou, H., Cai, Z., Wu, Y., Guo, Runtao, Han, T., Xue, J., Boucher, O., Boucher, E., Chevallier, F., Tanaka, K., Wei, Y., Zhong, H., Kang, C., Zhang, N., Chen, B., Xi, F., Liu, M., Bréon, F.-M., Lu, Y., Zhang, Q., Guan, D., Gong, P., Kammen, D.M., He, K., Schellhuber, H.J., 2020b. Near-real-time monitoring of global CO<sub>2</sub> emissions reveals the effects of the COVID-19 pandemic. *Nat. Commun.* 11, 5172. <https://doi.org/10.1038/s41467-020-18922-7>.
- Lopez, M., Schmidt, M., Delmotte, M., Colomb, A., Gros, V., Janssen, C., Lehman, S.J., Mondelain, D., Perrussel, O., Ramonet, M., Xueref-Remy, I., Bousquet, P., 2013. CO, NO<sub>x</sub> and 13CO<sub>2</sub> as tracers for fossil fuel CO<sub>2</sub>: results from a pilot study in Paris during winter 2010. *Atmos. Chem. Phys.* 13, 7343–7358. <https://doi.org/10.5194/ACP-13-7343-2013>.
- Lorente, A., Boersma, K.F., Eskes, H.J., Veeffkind, J.P., van Geffen, J.H.G.M., de Zeeuw, M.B., Denier van der Gon, H.A.C., Beirle, S., Krol, M.C., 2019. Quantification of nitrogen oxides emissions from build-up of pollution over Paris with TROPOMI. *Sci. Rep.* 9, 20033. <https://doi.org/10.1038/s41598-019-56428-5>.
- Mahadevan, P., Wofsy, S., Matross, D., Xiao, X., Dunn, A., Lin, J.C., Gerbig, C., Munger, J. W., Chow, V.Y., Gottlieb, E., 2008. A Satellite-based Biosphere Parameterization for Net Ecosystem CO<sub>2</sub> Exchange: Vegetation Photosynthesis and Respiration Model (VPRM). <https://doi.org/10.1029/2006GB002735>.
- Maldonado-Pacheco, G., García-Reynoso, J.A., Stremme, W., Ruiz-Suárez, L.G., García-Yee, J.S., Clerbaux, C., Coheur, P.-F., 2021. Carbon monoxide emissions assessment by using satellite and modeling data: Central Mexico case study. *Atmosférica* 34, 157–170. <https://doi.org/10.20937/ATM.52696>.
- Marland, G., 2008. Uncertainties in accounting for CO<sub>2</sub> from fossil fuels. *J. Ind. Ecol.* 12, 136–139. <https://doi.org/10.1111/j.1530-9290.2008.00014.x>.
- Mitchell, L.E., Lin, J.C., Bowling, D.R., Pataki, D.E., Strong, C., Schauer, A.J., Bares, R., Bush, S.E., Stephens, B.B., Mendoza, D., Mallia, D., Holland, L., Gurney, K.R., Ehleringer, J.R., 2018. Long-term urban carbon dioxide observations reveal spatial and temporal dynamics related to urban characteristics and growth. *PNAS* 115, 2912–2917. <https://doi.org/10.1073/pnas.1702393115>.
- Miyazaki, K., Bowman, K., Sekiya, T., Takigawa, M., Neu, J.L., Sudo, K., Osterman, G., Eskes, H., 2021. Global tropospheric ozone responses to reduced NO<sub>x</sub> emissions linked to the COVID-19 worldwide lockdowns. *ScienceAdvances* 7, eabf7460. <https://doi.org/10.1126/sciadv.abf7460>.
- Mueller, K., Yadav, V., Lopez-Coto, I., Karion, A., Gourdji, S., Martin, C., Whetstone, J., 2018. Siting background towers to characterize incoming air for urban greenhouse gas estimation: a case study in the Washington, DC/Baltimore area. *J.Geophys.Res.* Atmos. 123, 2910–2926. <https://doi.org/10.1002/2017JD027364>.
- Nassar, R., Hill, T.G., McLinden, C.A., Wunch, D., Jones, D.B.A., Crisp, D., 2017. Quantifying CO<sub>2</sub> emissions from individual power plants from space. *Geophys. Res. Lett.* 44, 10045–10053. <https://doi.org/10.1002/2017GL074702>.
- Nassar, R., Mastrogiovanni, J.-P., Bateman-Hemphill, W., McCracken, C., MacDonald, C. G., Hill, T., O'Dell, C.W., Kiel, M., Crisp, D., 2021. Advances in quantifying power plant CO<sub>2</sub> emissions with OCO-2. *Remote Sens. Environ.* 264, 112579. <https://doi.org/10.1016/j.rse.2021.112579>.
- NCAR, 2014. NCAR Upper Air Database, 1920-Ongoing. Research Data Archive at the National Center for Atmospheric Research, Computational and Information Systems Laboratory, Boulder CO.
- Oda, T., Maksyutov, S., Andres, R.J., 2018. The open-source data inventory for anthropogenic carbon dioxide (CO<sub>2</sub>), version 2016 (ODIAC2016): a global, monthly fossil-fuel CO<sub>2</sub> gridded emission data product for tracer transport simulations and surface flux inversions. *Earth Syst. Sci. Data* 10, 87–107. <https://doi.org/10.5194/essd-10-87-2018>.
- O'Dell, C., Eldering, A., Wennberg, P., Crisp, D., Gunson, M., Fisher, B., Frankenberg, C., Kiel, M., Lindqvist, H., Mandrake, L., Merrelli, A., Natraj, V., Nelson, R., Osterman, G., Payne, V., Taylor, T., Wunch, D., Drouin, B., Oyafuso, F., Chang, A., McDuffie, J., Smyth, M., Baker, D., Basu, S., Chevallier, F., Crowell, S., Feng, L., Palmer, P., Dubey, M., Garcia, O., Griffith, D., Hase, F., Iraci, L., Kivi, R., Morino, I., Notholt, J., Ohyama, H., Petri, C., Roehl, C., Sha, M.K., Strong, K., Sussmann, R., Te, Y., Uchino, O., Velasco, V., 2018. Improved retrievals of carbon dioxide from Orbiting Carbon Observatory-2 with the version 8 ACOS algorithm. In: Faculty of Science, Medicine and Health - Papers: Part B, pp. 6539–6576. <https://doi.org/10.5194/amt-11-6539-2018>.
- Park, Hayoung, Jeong, S., Park, Hoonyoung, Labzovskii, L.D., Bowman, K.W., 2021. An assessment of emission characteristics of Northern Hemisphere cities using spaceborne observations of CO<sub>2</sub>, CO, and NO<sub>2</sub>. *Remote Sens. Environ.* 254, 112246. <https://doi.org/10.1016/j.rse.2020.112246>.
- Parrish, D.D., Kuster, W.C., Shao, M., Yokouchi, Y., Kondo, Y., Goldan, P.D., de Gouw, J. A., Koike, M., Shirai, T., 2009. Comparison of air pollutant emissions among mega-cities. *Atmos. Environ.* 43, 6435–6441. <https://doi.org/10.1016/j.atmosenv.2009.06.024>.

- Qian, H., Xu, S., Cao, J., Ren, F., Wei, W., Meng, J., Wu, L., 2021. Air pollution reduction and climate co-benefits in China's industries. *Nat.Sustain.* 4, 417–425.
- Rella, C.W., Chen, H., Andrews, A.E., Filges, A., Gerbig, C., Hatakka, J., Karion, A., Miles, N.L., Richardson, S.J., Steinbacher, M., Sweeney, C., Wastine, B., Zellweger, C., 2013. High accuracy measurements of dry mole fractions of carbon dioxide and methane in humid air. *Atmos.Meas.Tech.* 6, 837–860. <https://doi.org/10.5194/amt-6-837-2013>.
- Reuter, M., Buchwitz, M., Hilboll, A., Richter, A., Schneising, O., Hilker, M., Heymann, J., Bovensmann, H., Burrows, J.P., 2014. Decreasing emissions of NO<sub>x</sub> relative to CO<sub>2</sub> in East Asia inferred from satellite observations. *Nat.Geosci.* 7, 792–795. <https://doi.org/10.1038/ngeo2257>.
- Reuter, M., Buchwitz, M., Schneising, O., Krautwurst, S., O'Dell, C.W., Richter, A., Bovensmann, H., Burrows, J.P., 2019. Towards monitoring localized CO<sub>2</sub> emissions from space: co-located regional CO<sub>2</sub> and NO<sub>2</sub> enhancements observed by the OCO-2 and S5P satellites. *Atmos. Chem. Phys.* 19, 9371–9383. <https://doi.org/10.5194/acp-19-9371-2019>.
- Rodriguez Zas, J.A., Garcia Reynoso, J.A., 2021. Updating of the 2013 National Emissions Inventory for air quality modeling in Central Mexico. *Rev. Int. Contam. Ambiental* 37, 463–487. <https://doi.org/10.20937/RICA.53865>.
- Saw, G.K., Dey, S., Kaushal, H., Lal, K., 2021. Tracking NO<sub>2</sub> emission from thermal power plants in North India using TROPOMI data. *Atmos. Environ.* 259, 118514 <https://doi.org/10.1016/j.atmosenv.2021.118514>.
- Schuh, A.E., Otte, M., Lauvaux, T., Oda, T., 2021. Far-field biogenic and anthropogenic emissions as a dominant source of variability in local urban carbon budgets: a global high-resolution model study with implications for satellite remote sensing. *Remote Sens. Environ.* 262, 112473 <https://doi.org/10.1016/j.rse.2021.112473>.
- SEDEMA, 2018. *Inventario de emisiones de la Ciudad de México-2016: Contaminantes Criterio, Tóxicos y compuestos de Efecto Invernadero* (In Spanish).
- Shan, Y., Guan, D., Zheng, H., Ou, J., Li, Y., Meng, J., Mi, Z., Liu, Z., Zhang, Q., 2018. China CO<sub>2</sub> emission accounts 1997–2015. *Sci. Data* 5, 170201. <https://doi.org/10.1038/sdata.2017.201>.
- Skamarock, C., Klemp, B., Dudhia, J., Gill, O., Barker, D., Duda, G., Huang, X., Wang, W., Powers, G., 2008. A Description of the Advanced Research WRF Version 3. <https://doi.org/10.5065/D68S4MVH>.
- Taylor, T.E., Eldering, A., Merrelli, A., Kiel, M., Somkuti, P., Cheng, C., Rosenberg, R., Fisher, B., Crisp, D., Basilio, R., Bennett, M., Cervantes, D., Chang, A., Dang, L., Frankenberg, C., Haemmerle, V.R., Keller, G.R., Kurosu, T., Laughner, J.L., Lee, R., Marchetti, Y., Nelson, R.R., O'Dell, C.W., Osterman, G., Pavlick, R., Roehl, C., Schneider, R., Spiers, G., To, C., Wells, C., Wennberg, P.O., Yelamanchili, A., Yu, S., 2020. OCO-3 early mission operations and initial (vEarly) XCO<sub>2</sub> and SIF retrievals. *Remote Sens. Environ.* 251, 112032 <https://doi.org/10.1016/j.rse.2020.112032>.
- UNFCCC, 2015. *Paris Agreement*.
- Wang, R., Tao, S., Ciais, P., Shen, H.Z., Huang, Y., Chen, H., Shen, G.F., Wang, B., Li, W., Zhang, Y.Y., Lu, Y., Zhu, D., Chen, Y.C., Liu, X.P., Wang, W.T., Wang, X.L., Liu, W.X., Li, B.G., Piao, S.L., 2013. High-resolution mapping of combustion processes and implications for CO<sub>2</sub> emissions. *Atmos. Chem. Phys.* 13, 5189–5203. <https://doi.org/10.5194/acp-13-5189-2013>.
- Xie, X., Weng, Y., Cai, W., 2018. Co-benefits of CO<sub>2</sub> mitigation for NO<sub>x</sub> emission reduction: a research based on the DICE model. *Sustainability* 10, 1109. <https://doi.org/10.3390/su10041109>.
- Yadav, V., Ghosh, S., Mueller, K., Karion, A., Roest, G., Gourdji, S.M., Lopez-Coto, I., Gurney, K.R., Parazoo, N., Verhulst, K.R., Kim, J., Prinzievalli, S., Fain, C., Nehrkorn, T., Mountain, M., Keeling, R.F., Weiss, R.F., Duren, R., Miller, C.E., Whetstone, J., 2021. The impact of COVID-19 on CO<sub>2</sub> emissions in the Los Angeles and Washington DC/Baltimore metropolitan areas. *Geophys. Res. Lett.* 48, e2021GL092744 <https://doi.org/10.1029/2021GL092744>.
- Yang, E.G., Kort, E.A., Wu, D., Lin, J.C., Oda, T., Ye, X., Lauvaux, T., 2020. Using space-based observations and Lagrangian modeling to evaluate urban carbon dioxide emissions in the Middle East. *J.Geophys.Res.Atmos.* 125, e2019JD031922 <https://doi.org/10.1029/2019JD031922>.
- Ye, X., Lauvaux, T., Kort, E.A., Oda, T., Feng, S., Lin, J.C., Yang, E.G., Wu, D., 2020. Constraining fossil fuel CO<sub>2</sub> emissions from urban area using OCO-2 observations of total column CO<sub>2</sub>. *J.Geophys.Res.Atmos.* 125, e2019JD030528 <https://doi.org/10.1029/2019JD030528>.
- Zhang, R., Tie, X., Bond, D.W., 2003. Impacts of anthropogenic and natural NO<sub>x</sub> sources over the U.S. on tropospheric chemistry. *PNAS* 100, 1505–1509. <https://doi.org/10.1073/pnas.252763799>.
- Zheng, T., Nassar, R., Baxter, M., 2019. Estimating power plant CO<sub>2</sub> emission using OCO-2 XCO<sub>2</sub> and high resolution WRF-Chem simulations. *Environ. Res. Lett.* 14, 085001 <https://doi.org/10.1088/1748-9326/ab25ae>.
- Zheng, B., Geng, G., Ciais, P., Davis, S.J., Martin, R.V., Meng, J., Wu, N., Chevallier, F., Broquet, G., Boersma, F., Lin, J., Guan, D., Lei, Y., He, K., Zhang, Q., A, R.van der, 2020. Satellite-based estimates of decline and rebound in China's CO<sub>2</sub> emissions during COVID-19 pandemic. *Sci. Adv.* 6, eabd4998 <https://doi.org/10.1126/sciadv.abd4998>.
- Zhou, Y., Williams, C.A., Lauvaux, T., Feng, S., Baker, I.T., Wei, Y., Denning, A.S., Keller, K., Davis, K.J., 2020. ACT-America: Gridded Ensembles of Surface Biogenic Carbon Fluxes, 2003-2019.